JOURNAL OF PETROLOGY | VOLUME 38 | NUMBER 9 | PAGES 1225–1253 | 1997

Petrogenesis of a Phonolite–Trachyte Succession at Mount Sidley, Marie Byrd Land, Antarctica

KURT S. PANTER[1]*, PHILIP R. KYLE[1] AND JOHN L. SMELLIE[2]

[1]DEPARTMENT OF EARTH AND ENVIRONMENTAL SCIENCE, NEW MEXICO INSTITUTE OF MINING AND TECHNOLOGY, SOCORRO, NM 87801, USA

[2]BRITISH ANTARCTIC SURVEY, HIGH CROSS, MADINGLEY ROAD, CAMBRIDGE CB3 0ET, UK

RECEIVED APRIL 22, 1996 REVISED TYPESCRIPT ACCEPTED APRIL 11, 1997

The 1·5 Ma evolution of the Late Pliocene (5·7 to 4·2 Ma) Mt Sidley volcano, Marie Byrd Land, is examined using major and trace elements, Sr, Nd, O and Pb isotopic data. A large (5 km × 5 km) breached caldera exposes lavas and tephras, deep within Mt Sidley, and allows its magmatic evolution to be elucidated. Two alkaline rock series are distinguished: (a) a strongly silica-undersaturated basanite to phonolite series; (b) a more silica-saturated to -oversaturated alkali basalt to trachyte series. Rock compositions in both series fall within a narrow range of $^{87}Sr/^{86}Sr_i$ *(0·7028–0·7032),* $^{143}Nd/^{144}Nd_i$ *(0·51285–0·51290) and* $\delta^{18}O$ *(5·0–6·0‰), and with* $^{206}Pb/^{204}Pb$ *(>19·5), suggest an asthenospheric source containing a strong mantle plume component. Partial melting models require* $\leq 2\%$ *melting to produce primary basanite and* $\geq 5\%$ *melting to produce alkali basalt from the same mantle source. The differentiation of the phonolitic series is modeled by fractionation of diopside, olivine, plagioclase, titaniferous magnetite, nepheline and/or apatite from basanite to derive 35% mugearite, 25% benmoreite and 20% phonolite as residual liquids. Fractional crystallization of a similar mineral assemblage from alkali basalt is modeled for compositions in the trachyte series. However, many trachytes have variable* $^{87}Sr/^{86}Sr_i$ *(0·7033–0·7042), low* $^{143}Nd/^{144}Nd_i$ *(0·51280–0·51283), high* $\delta^{18}O$ *(6·5–8·4‰) and are silica oversaturated, suggesting they are contaminated by crust. The trachytes evolved by a two-step assimilation–fractional crystallization process (AFC). The first step involved contamination of alkali basalt by calc-alkaline granitoids within the middle crust where high assimilation to crystallization rates (high-r AFC) produced trachytic magmas characterized by depletions in Ta and Nb relative to K and Rb. The second step involved further fractionation of these magmas by low-r AFC within the upper crust to produce another suite of trachytes showing extreme incompatible element enrichment (e.g. Zr>2000 p.p.m. and Th>100 p.p.m.).*

KEY WORDS: *alkaline magmas; AFC; magma commingling; Marie Byrd Land; volcanism*

INTRODUCTION

Mt Sidley, an Early Pliocene composite volcano, is at the south end of the Executive Committee Range, a 100-km chain of volcanoes in west Antarctica (Fig. 1). The Marie Byrd Land volcanic province lies within a broad region of extended crust and young (~35 Ma to active at present) alkaline volcanism that occurs along the Pacific margin of Antarctica from Ellsworth Land to the northern coast of Victoria Land (~3500 km). It is one of the world's major continental rift systems (LeMasurier & Thomson, 1990). In Marie Byrd Land, 18 large composite centers rise above the West Antarctic Ice Sheet, but few have adequate ice-free exposures to permit comprehensive study of their eruptive history and petrogenesis. At Mt Sidley, a large breached caldera has exposed volcanic strata deep within its interior, revealing a long and complex history of eruption (Panter *et al.*, 1994).

Volcanic rocks in the Marie Byrd Land province are dominantly alkaline. Geochemical studies of other similar

*Corresponding author.

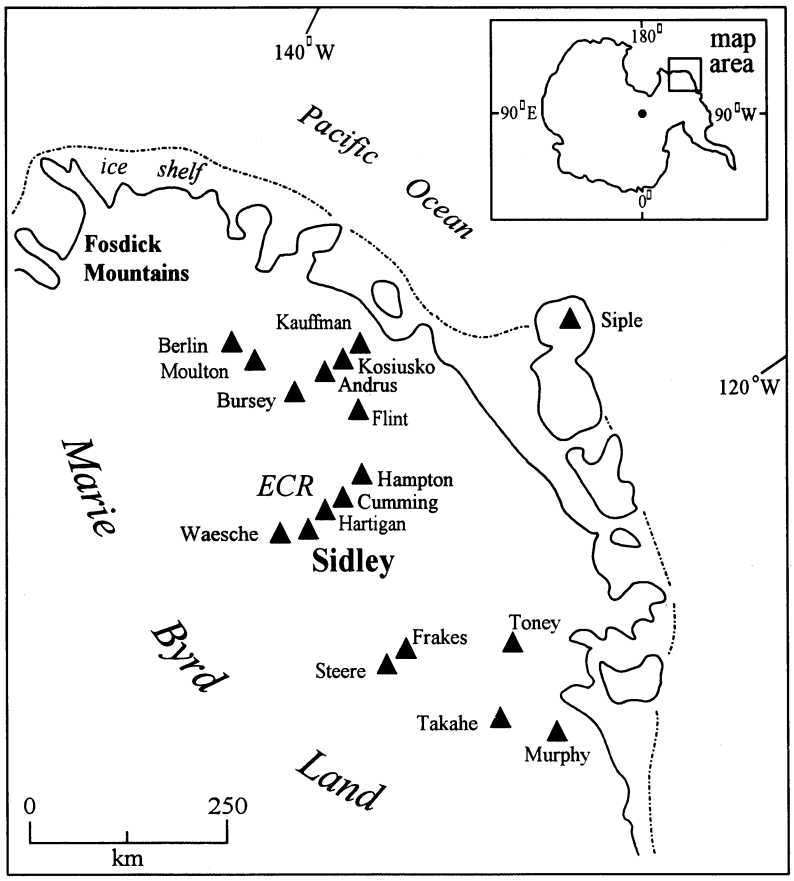

Fig. 1. Major volcanoes in Marie Byrd Land, Antarctica. ECR, Executive Committee Range.

continental alkaline suites have shown that alkaline rocks evolve along a strongly silica-undersaturated basanite to phonolite lineage and a more silica-saturated alkali basalt to trachyte lineage (Wilson *et al.*, 1995). Only rarely have the two lineages been traced through a suite of coexisting rocks at a single volcano, often because of the preponderance of either basaltic or highly evolved compositions and the dearth of intermediate rock-types. Petrogenetic studies of closely associated silica-undersaturated and silica-oversaturated rock suites commonly invoke complex open system processes to explain their origin from a common parent (e.g. Turbeville, 1993; Freundt & Schmincke, 1995) and specifically, the assimilation of crust by mantle-derived silica-undersaturated melts to produce oversaturated alkaline magmas (e.g. Foland *et al.*, 1993; Macdonald *et al.*, 1995).

Here we present geochemical data to examine the petrogenesis of phonolitic and trachytic magmas at Mt Sidley. Our objective is to determine the genetic relationships between silica-undersaturated and silica-saturated to -oversaturated rocks within the volcanic succession. Theoretical modeling of geochemical variations addresses both open and closed system processes and reveals a complex magmatic history involving variable degrees of mantle partial melting, magma mixing or mingling, fractional crystallization and crustal assimilation.

VOLCANIC GEOLOGY

Mt Sidley (4181 m) is a large (>200 km^3) volcano composed primarily of phonolitic and trachytic lavas. Mapping, stratigraphy and 14 high-precision $^{40}Ar/^{39}Ar$ ages reveal a complex, polygenetic volcano built in successive stages from 5·7 to 4·2 Ma (Panter *et al.*, 1994). Mt Sidley comprises several coalesced phonolitic volcanoes flanked by many smaller centers. Changes in magma composition coincide with a southward migration of volcanic activity, occurring in four main stages. In stage I (5·7–4·8 Ma), three major volcano-building episodes (Byrd, Weiss and Sidley; Table 1), each culminated with caldera formation and produced >1000 m of phonolite–tephriphonolite lavas. Trachyte lavas, domes and pyroclastics erupted during stage II (4·6-4·5 Ma) were centered 5–6 km to

Table 1: Summary of petrographic features for Mt Sidley rocks; samples grouped by stage and episode of activity (Panter et al.*, 1994)*

Stage	Episode	Rock type	Major minerals (≥5%)	Minor minerals	Accessory	Phenocryst %	Texture
IV	Parasitic Cones	basanite	Plag + Ol + Cpx	—	Ox	5–30	p→fp, t
		Trachyte tephras:					
III	Doumani	welded fall	Akf	Cpx + Ol	Ox	10–15	w, vtph
	Activity	ignimbrite (pumice)	—	Akf + Cpx	—	≤1	vtph
		benmoreite	Akf	Ol≫Cpx≫mica	Ox	30	fp, t
		phonotephrite	Ol	Plag>mica	Ox	10	fp→mp
		mugearite	Plag>Ol	mica + Cpx	Ox	40	p
II	Pirrit Activity	trachyte commingled lavas:	Akf + Cpx	Ol + Plag≫Amp	Ox	5–30	gp→p, t
		trachytic	Akf	Cpx + Ol + Amp	Ox	10–25	cp→p
	Sidley Volcano	phonolite	Akf	Cpx + Ol + Fspth	Ox + Ap	5–45	cp→fp, amg, vtph
	Weiss	phonolite	Akf	Fspth + Plag + Cpx + Ol	Ox + Ap	1–10	fp→mp, t, amg
I	Volcano	*Intrusives:* phonolite	Akf	Ol≫Cpx	Ox>Ap	25	vtph
		benmoreite	Akf>Fspth>Cpx	Ol	Ox>Ap	—	so
	Byrd Volcano	tephriphonolite–phonolite	Akf + Fspth	Plag + Ol + Cpx	Ox + Ap	30–50	cp, t, amg

Akf, alkali feldspar; Fspth, feldspathoid; Cpx, clinopyroxene; Ol, olivine; Plag, plagioclase; Ox, Fe–Ti oxides; Ap, apatite; Amp, alkali-amphibole; mica, brownish red mica (phlogopite–biotite). cp, coarsely porphyritic (>1 cm); p, porphyritic (>5 mm); fp, finely porphyritic (<5 mm); mp, microporphyritic (<2 mm); gp, glomeroporphyritic; amg, amygdaloidal; t, trachytic; w, welded; vtph, vitrophyric; so, subophitic. The commingled lavas in stage II refer to mafic inclusion-bearing lavas (see text).

the south of the stage I vents. A black, compositionally heterogeneous (phonolite–trachyte), lapilli tuff fall deposit in the southwestern caldera wall defines the shift from phonolitic to trachytic magmatism. The black pyroclastic fall deposit passes up into a 70 m thick unit of alternating lithic breccias and trachyte lavas. The transition from the fall deposit into the trachytic sequence (dark gray unwelded cindery scoria→fiamme-like flattened scoria→light gray strongly welded tuff→cream-colored thinly foliated lavas), is interpreted to be the product of a single eruptive phase (Smellie *et al.*, 1990). In the upper portion of this cogenetic sequence, several trachyte lavas contain partially resorbed mafic inclusions (commingled lavas; Panter *et al.*, 1994, fig. 7b). Stage III (4·4-4·3 Ma) began with an explosive paroxysmal eruption of trachytic magmas (conformable units; lithic-rich welded pyroclastic fall and unwelded ignimbrite) and catastrophic landslide of the southern flank of the volcano, leading to the formation of the 5 km × 5 km, 1200 m deep Weiss Amphitheater. This was followed, 9 km south of stage I activity, by a final pulse of differentiated magmas, in which mugearite and benmoreite lavas were erupted. Volcanism ceased at 4·2 Ma (stage IV) following the eruption of xenolith-bearing parasitic cones of basanite.

PETROGRAPHY AND MINERAL CHEMISTRY

Mt Sidley volcanic rocks are strongly porphyritic and their petrographic features are summarized in Table 1. Minerals were analyzed by a JEOL-733 electron microprobe, using 15 kV accelerating potential, 12-13 nA sample current and 1-10 μm electron beam.

Olivine

Olivine phenocrysts occur in all rock types, ranging from 10% (modal) in mafic and intermediate lavas to ≤2 % in phonolites and trace amounts in trachytes. Olivine ranges from Fo_{86} within mafic inclusion-bearing trachytic

lavas to Fo_1 in trachytes (Fig. 2; Table 2). Olivine phenocrysts are often normally zoned with homogeneous cores mantled by more fayalitic rims. Reversely zoned olivine occurs in several phonolitic lavas of stage I and within mafic inclusion-bearing trachytic lavas of stage II. The outermost rims of reversely zoned olivines in phonolites are enriched in MgO ($\leq 0{\cdot}6$ wt %) and CaO ($\leq 0{\cdot}1$ wt %) with depletions in FeO ($\leq 1{\cdot}0$ wt %) and MnO ($\leq 0{\cdot}2$ wt %) relative to their cores. The zoning suggests an abrupt compositional change in the coexisting melt during olivine crystallization.

Clinopyroxene

The clinopyroxene phenocrysts plot mostly in the Ca–Mg–Fe quadrilateral (Fig. 2), although some lie above the CaMg-$CaFe^{2+}$ join. Diopsides in basanite are subsilicic (<1·75 Si atoms per formula unit, a.f.u.) aluminian, calcian (Ca>0·9 a.f.u.) and magnesian (Mg>0·9 a.f.u.). Diopside and calcian diopside occur in phonolites and ferroan ($Fe^{2+}>0{\cdot}5$ a.f.u.) hedenbergite within trachytes and mugearites (Fig. 2). Clinopyroxenes within mafic inclusion-bearing trachytic lavas show a large compositional range (Fig. 2) from subsilicic aluminum diopside and magnesian diopside in mafic inclusions to ferroan hedenbergite within the felsic host.

Pyroxene phenocrysts in mafic inclusions from trachytic lavas have Fe-rich rims relative to cores ($\Delta = 14$ wt % FeO), whereas pyroxene in the trachytic host is reversely zoned with MgO content increasing (from ~1 to 4 wt %) and FeO decreasing (from ~28 to 25 wt %) from cores to rims. Pyroxenes in several stage I phonolitic lavas are reversely zoned and phenocrysts within one flow (K144, Table 2) have significantly higher *mg*-numbers for rims relative to cores, indicating disequilibrium conditions during crystal growth.

Feldspars

Feldspar phenocrysts (Table 2) range from labradorite ($An_{54}Ab_{44}Or_2$) in basanites and mugearites to sodic sanidine ($An_2Ab_{54}Or_{44}$) in tephriphonolites and trachytes. Potassic anorthoclase in mafic inclusion-bearing trachytic lavas have a limited compositional range ($An_{<7}Ab_{55-66}Or_{30-42}$) and plot near the thermal minimum of the binary system An–Or (Tuttle & Bowen, 1958). This suggests the feldspar precipitated as a hypersolvus phase during late-stage crystallization of highly fractionated liquids (Brown, 1993).

In trachytic lavas, feldspars are normally zoned with Or-rich rims. Pronounced, oscillatory normal-zoning of anorthoclase in a benmoreite stock reveals a pronounced increase in the Or molecule between cores and rims (sample K166; Table 2). Feldspars in phonolitic lavas from the Sidley succession display discontinuously zoned rims enriched in the An component. The occurrence of reversely zoned feldspars in these lavas is consistent with compositional reversals in coexisting clinopyroxenes and olivines.

Amphibole and mica

Strongly pleochroic (brownish green, blue) alkali amphibole occurs as small ($\leq 0{\cdot}3$ mm) euhedral microphenocrysts within some trachytes. Alkali amphibole is the most abundant in mafic inclusion-bearing lavas, where it is found predominantly as subhedral to euhedral crystals within vesicles. Brownish red mica occurs within several mafic to intermediate lavas (stage III, Table 1).

Stoichiometric amphiboles are arfvedsonite [classification of (Mogessie *et al.*, 1990)]. Arfvedsonite is a product of magmatic-subsolidus processes, principally found in differentiated alkaline magmas (Ernst, 1962; Wolff & Toney, 1993). Compositional trends towards Ca + Mg depletion (Fig. 2) and alkali enrichment are similar to the observed amphibole trends within the alkaline Ilímaussaq complex (Larsen, 1976) and the Kungnat Field, south Greenland (Stephenson & Upton, 1982). Such changes in amphibole chemistry can be partly explained by the coupled substitution of (Na, K) + Si for Ca + Al, occurring when residual liquids become peralkaline.

Mafic inclusion-bearing trachytic lavas: evidence for magma commingling

The commingling of mafic and felsic magmas forms heterogeneous mixtures which often produce banded or inclusion-bearing rock units. The textural features exhibited by the mafic inclusion-bearing trachytic lavas of stage II are consistent with an origin by magma commingling. Mafic inclusions (typically ≤ 10 cm) are rounded and vesicular with well-developed crenulated surfaces embayed by the trachytic host. The contact interface between the inclusions and the host is sharp on a macroscopic scale; however, petrographic observations reveal fine-scale dissemination of inclusion material within the host and abundant amygdules containing feldspar and alkali amphibole. Amphibole in mafic inclusions becomes increasingly rare within several millimeters of the contact (unless vesicles are present) but can be found several times further within the host. The textural relationships suggest that amphibole crystallized from a vapor phase which exsolved from the magmas during mingling.

The interaction of mafic and felsic magmas can produce complex disequilibrium textures in minerals (e.g. Stimac & Pearce, 1992). Large (up to 1 cm) anorthoclase crystals

Table 2: Representative electron microprobe analyses of phenocrysts

	basanite K168				mugearite K93				benmoreite K166				phonolite K120			
	Ol core	Cpx core	Plag core	Timt core	Ol core	Cpx core	Plag core	Timt core	Cpx core	Cpx rim	Akf core	Akf rim	Ol core	Cpx core	Akf core	Timt core
SiO_2	38·26	54·15	52·83	0·15	33·83	49·06	56·19	0·16	51·13	49·72	65·90	66·78	32·81	50·97	63·77	—
TiO_2	—	0·30	0·09	0·79	—	0·52	—	26·61	0·55	0·60	—	—	—	0·80	—	24·81
Al_2O_3	—	0·67	29·06	58·54	—	0·46	27·13	1·67	1·15	1·01	20·02	18·52	—	2·21	21·73	2·35
FeO*	23·23	2·73	0·27	22·43	45·78	27·06	0·30	66·79	15·27	21·78	0·19	0·13	49·37	12·15	—	68·58
MnO	0·31	0·16	—	0·39	0·94	0·68	—	0·72	0·46	0·73	—	—	2·09	0·53	—	1·63
MgO	38·27	17·16	—	16·86	19·23	2·48	—	1·54	8·95	4·45	—	—	15·24	10·68	—	1·63
CaO	0·14	24·25	11·23	—	0·33	20·74	9·51	—	22·22	19·44	1·38	0·15	0·54	21·99	3·28	—
Na_2O	—	0·26	6·39	—	—	0·62	5·82	—	0·67	1·74	7·28	5·64	—	0·82	7·82	—
K_2O	—		0·25	—	—	—	0·35	—	—	—	5·24	8·31	—	—	2·88	—
sum	100·21	99·68	100·12	99·15	100·11	101·62	99·30	97·49	100·40	99·47	100·01	99·53	100·05	100·15	99·48	99·00
mg-no.	75	94	An_{49}	65	43	15	An_{46}	5	54	30	Or_{30}	Or_{49}	35	65	Or_{16}	5

	phonolite K144						trachyte K66			commingled lavas K63 and JG025						
	Ol core	Ol rim	Cpx core	Cpx rim	Akf core	Timt core	Ol core	Cpx core	Akf core	Ol-i core	Ol-i rim	Cpx-h core	Cpx-h rim	Akf-h core	Timt-h core	Amp-h core
SiO_2	33·02	32·56	51·15	50·76	63·32	0·17	30·36	48·59	66·47	39·50	32·78	48·07	49·24	67·76	0·19	48·67
TiO_2	—	—	0·53	0·81	—	22·10	—	0·46	—	—	—	0·45	0·35	—	23·68	2·99
Al_2O_3	—	—	1·55	2·16	22·18	2·12	—	0·43	18·82	—	—	0·38	0·40	18·90	1·13	0·60
FeO*	50·79	49·8	14·07	13·51	0·23	71·19	64·50	26·93	0·17	14·45	52·41	28·06	24·62	0·27	71·42	33·72
MnO	2·39	2·2	0·64	0·6	—	1·37	5·14	1·00	—	0·21	1·96	0·84	0·92	—	1·18	0·92
MgO	13·65	14·23	9·19	9·82	—	1·56	0·81	1·83	—	46·03	12·86	0·86	3·48	—	0·58	1·31
CaO	0·65	0·73	21·65	22·19	3·68	0·07	0·22	20·25	0·42	0·25	0·37	20·20	20·08	0·19	—	3·97
Na_2O	—	—	0·84	0·85	7·72	—	—	0·55	6·81	—	—	0·54	0·64	7·29	—	6·33
K_2O	—	—	—	—	2·56	—	—	—	6·72	—	—	—	—	5·97	—	1·25
sum	100·50	99·52	99·62	100·70	99·69	98·58	101·03	100·04	99·41	100·44	100·38	99·40	99·73	100·38	98·18	99·76
mg-no.	32	34	56	62	Or_{15}	5	2	11	Or_{39}	85	30	5	21	Or_{35}	2	6

Ol, olivine; Cpx, clinopyroxene; Plag, plagioclase; Akf, alkali feldspar (anorthoclase); Timt, titanomagnetite. Commingled lavas: i, mafic inclusion; h, trachytic host. —, not determined or not detected.

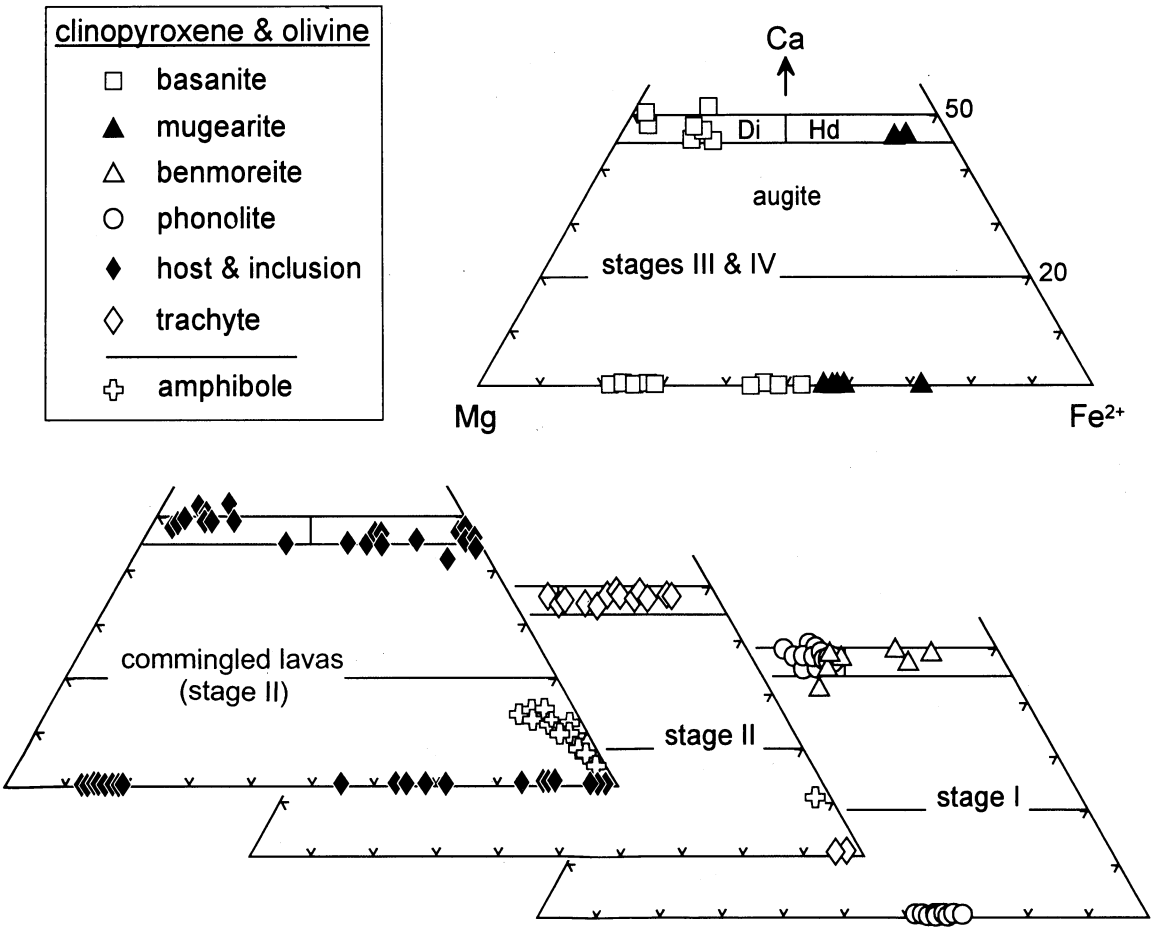

Fig. 2. Electron microprobe analyses of clinopyroxene, olivine and amphibole phenocrysts plotted in terms of atomic % Ca, Mg, Fe^{2+}. Compositions of olivines plot along the Mg–Fe^{2+} join and clinopyroxenes are shown relative to fields for diopside (Di), hedenbergite (Hd) and augite (Morimoto *et al.*, 1988). Clinopyroxenes in benmoreite (△) are from stage I intrusion. The 'commingled lavas' refer to mafic inclusion-bearing trachytic lavas of stage II (see text).

within the mafic inclusions indicate both mechanical transfer (e.g. Gourgaud, 1991) and chemical diffusion between magmas. Phenocrysts of alkali feldspar within the trachytic host have rounded and embayed crystal forms and are considered to be a product of simple dissolution during rapid heating by mafic magmas. A rapid increase in temperature is also recorded by compositional reversals in olivine and clinopyroxene phenocrysts within the host (discussed above). Phenocrysts within the mafic inclusions are normally zoned, indicating rapid undercooled crystallization of mafic magmas.

WHOLE-ROCK GEOCHEMISTRY

Representative whole-rock samples from Mt Sidley and from the neighboring and younger (<2 Ma) Mt Waesche volcano were analyzed by X-ray fluorescence (XRF) and instrumental neutron activation analysis (INAA). Major element data used in plots are recalculated on a 100% volatile-free basis with total Fe as FeO. Representative analyses are given in Table 3.

Neodymium isotopes (Table 4) were analyzed on a five-collector VG Isotopes 354 mass spectrometer. Nd data were normalized to a $^{144}Nd/^{146}Nd$ of 0·7219. The J&M in-house standard was used to correct data to an equivalent value of 0·511850 for the La Jolla standard. Analyses of BCR-1 gave a $^{143}Nd/^{144}Nd$ ratio of $0{\cdot}512628 \pm 10$ ($n=3$) and for JB-1 $0{\cdot}512780 \pm 41$ ($n=6$). Nd and Sm concentrations were determined by isotope dilution, and gave Sm/Nd ratios averaging 0·2279 for BCR-1 and 0·1933 for JB-1. Strontium isotopes (Table 4) were analyzed on a Finnegan MAT 262 instrument using static multiple collection. Long-term drift (caused

Table 3: Representative analyses of whole rocks from Mt Sidley and Mt Waesche

	Mt Sidley rocks																	Mingled or mixed compositions					Mt Waesche rocks					
Sample:	K109	MB27.5	K133	K095	MB32.11	K093	K099	K166	K097	K108	MB42.3	K144	K149	MB35.2	K055	MB33.8	MB33.3	K063A	K063B	MB35.5	MB33.11	MB38.3	MB4.1	K19	MB21.1	K01	MB11.2	MB15.1
Rock type:	bas	bas	bas	bas	mug	mug	mug	ben	ben	tphn	tphn	phn	phn	phn	trac	trac	trac	trac	ben	phn	trac	trac-phn	akb	akb	mug	phntph	tphn	trac
Group:	stage IV	stage IV	stage IV	stage IV	DPM	SFM	SFM	stage I	stage IV	Bv	Sv	Sv	Sv	Sv	*LT*	*HT*	*HT*	CL-host	CL-incl	bf	bf	bf						
SiO_2	44·67	44·71	45·88	47·73	50·62	51·31	51·38	55·17	55·75	55·90	55·97	56·12	56·12	57·02	61·94	67·57	68·30	65·88	57·22	56·71	59·73	59·38	45·62	45·84	50·39	51·59	55·97	59·71
TiO_2	3·03	3·15	3·05	2·48	1·75	1·57	1·54	0·96	0·95	1·26	0·69	0·61	0·65	0·25	0·47	0·21	0·26	0·38	1·12	0·19	0·75	0·77	2·03	2·55	1·77	1·66	1·02	0·60
Al_2O_3	15·03	15·68	16·11	17·36	16·71	16·92	16·91	17·62	17·41	16·62	19·65	19·75	19·71	19·17	17·87	13·58	13·17	14·88	15·84	19·49	17·62	17·32	16·54	15·03	18·42	17·41	17·38	17·84
Fe_2O_3	13·30	13·65	13·65	12·53	10·24	13·70	14·08	8·67	11·20	10·07	6·75	6·78	6·42	7·17	5·51	5·92	5·84	5·46	7·86	7·15	7·36	7·20	12·38	12·87	10·55	11·47	8·87	7·53
MnO	0·17	0·18	0·21	0·19	0·17	0·24	0·25	0·23	0·25	0·31	0·20	0·20	0·20	0·25	0·16	0·16	0·15	0·12	0·12	0·25	0·19	0·19	0·18	0·19	0·18	0·27	0·23	0·23
MgO	8·35	7·44	5·84	5·18	4·48	2·49	2·30	1·23	1·13	1·03	0·59	0·63	0·67	0·04	0·29	—	—	0·35	3·31	—	0·46	0·34	7·63	9·26	3·01	2·00	1·35	0·29
CaO	9·33	9·11	7·95	7·30	7·11	5·22	5·17	3·44	3·71	2·87	2·51	2·11	2·72	1·43	2·04	0·80	0·70	1·20	4·43	1·20	2·28	1·96	10·92	9·68	8·53	5·79	3·54	2·27
Na_2O	4·42	4·65	5·40	5·16	4·79	5·94	6·21	5·71	6·54	7·86	6·65	8·77	8·42	9·06	6·81	5·98	6·07	6·48	5·61	9·41	5·19	6·75	3·31	3·55	5·35	7·06	7·90	7·88
K_2O	1·45	1·43	1·96	1·63	2·13	2·27	2·25	4·76	2·92	4·12	4·93	5·19	4·83	5·19	4·82	4·91	4·98	5·08	4·03	5·39	5·71	5·68	0·58	1·17	1·53	2·25	3·71	3·61
P_2O_5	0·58	0·76	0·86	0·61	0·47	1·13	1·27	0·35	0·58	0·46	0·32	0·21	0·24	0·15	0·11	0·09	0·08	0·01	0·13	0·12	0·21	0·21	0·48	0·59	0·53	0·56	0·37	0·19
LOI	0	0	0	0	1·13	0	0	1·74	0	0	2·17	0	0·00	0·41	0·08	0·32	0·21	0	0·05	0·24	0·95	0·32	0·40	0	0	0	0	0·10
total	100·33	100·76	100·91	100·17	99·60	100·79	101·36	99·88	100·44	100·50	100·43	100·37	99·98	100·14	100·10	99·54	99·76	99·84	99·72	100·15	100·45	100·12	100·07	100·73	100·26	100·06	100·34	100·25
mg-no.	55	52	46	45	46	26	24	22	17	17	15	16	17	1	9	—	—	11	45	—	11	9	55	59	36	26	23	7
Sc	21·8	20·6	17·3	15·0	16·7	6·5	5·5	5·3	6·1	6·4	2·7	2·7	2·7	1·1	3·2	0·3	0·4	2·5	12·7	0·8	4·9	5·2	26·0	25·0	16·0	8·0	6·0	2·0
V	193	191	137	143	113	11	4	3	9	6	1	—	—	—	1	13	1	3	78	—	—	—	223	202	88	2	22	1
Cr	145	68	43	—	60	—	—	—	—	—	—	—	—	—	—	—	—	15	93	—	—	—	158	412	10	—	—	—
Ni	136	111	54	31	40	11	9	4	6	5	4	4	5	6	4	10	9	8	48	7	7	6	80	180	20	5	12	5
Cu	80	93	49	47	48	39	42	16	25	16	20	17	16	15	13	22	14	9	57	14	26	15	73	84	59	32	26	15
Zn	87	85	92	81	86	91	97	109	88	169	116	110	126	185	90	271	212	130	107	186	133	133	84	91	88	11	126	129
Ga	22	19	20	20	23	24	20	29	26	36	42	31	31	44	31	48	46	34	24	44	33	36	23	19	23	22	29	31
Rb	35	32	55	44	40	56	56	176	87	105	203	227	205	249	214	672	593	244	96	275	395	284	11	25	31	51	90	80
Sr	752	877	950	715	492	734	756	199	562	210	264	165	272	49	220	—	—	23	176	1	76	43	494	581	513	589	201	221
Y	25	25	34	30	30	40	41	79	41	82	66	68	73	107	64	210	190	82	40	109	93	84	22	27	34	47	62	63
Zr	254	241	334	307	268	433	443	1258	584	995	1138	1478	1330	1869	923	2291	2260	963	308	2018	1981	1619	135	253	269	364	674	673
Nb	60	59	96	71	58	93	97	215	117	199	252	263	259	341	146	516	405	154	59	369	355	281	27	52	59	102	132	124
As	1·0	1·2	1·0	—	2·0	—	1·3	—	2·1	3·3	4·1	6·9	5·5	8·9	7·7	13·3	—	1·7	3·1	8·7	5·0	4·9	0·4	—	1·1	1·5	2·4	3·8
Sb	—	—	—	—	0·0	0·1	0·1	0·1	0·2	0·2	0·5	0·5	0·4	0·5	0·3	1·1	0·6	0·2	0·0	0·6	0·5	0·4	—	—	—	0·1	0·2	—
Cs	0·58	0·42	0·59	0·55	0·50	0·52	0·44	5·84	0·91	1·06	8·94	6·46	5·58	4·99	4·18	34·10	10·69	5·84	4·15	6·27	18·45	6·17	0·20	0·50	0·40	0·60	1·20	1·70
Ba	344	419	666	404	500	662	645	583	891	717	571	350	519	105	566	—	—	—	264	—	450	301	199	250	457	703	668	1023
La	40·70	42·9	68·80	52·50	42·50	80·60	83·00	131·70	101·10	112·60	118·65	117·70	119·40	172·65	109·40	331·00	270·80	122·50	48·20	176·80	181·85	135·75	20·20	39·00	43·00	70·00	85·80	81·50
Ce	82·8	84·6	134·0	99·2	82·8	153·9	160·9	238·9	187·1	214·6	238·5	211·5	217·4	312·0	199·1	600·0	494·0	235·6	94·6	325·0	344·0	245·8	44·8	80·9	87·5	135·5	166·0	161·3
Nd	32·0	36	51·0	39·0	32·5	62·0	60·0	82·0	67·0	83·0	71·0	64·0	71·0	105·0	66·0	175·0	181·0	77·5	40·0	112·0	106·0	84·0	21·0	34·0	32·0	53·0	57·0	63·0
Sm	7·60	7·88	11·27	7·80	7·23	11·42	12·00	15·33	11·31	16·80	13·06	12·60	13·50	19·41	13·65	32·75	34·20	16·81	8·16	19·88	18·81	15·26	5·03	7·29	7·46	11·37	13·30	12·43
Eu	2·43	2·57	3·20	2·39	2·26	3·31	3·51	3·41	3·11	4·79	2·76	2·41	2·73	1·77	2·20	0·67	0·49	0·58	1·51	1·27	2·32	1·95	1·81	2·30	2·69	3·64	2·82	3·54
Tb	0·96	0·93	1·24	1·00	0·94	1·31	1·33	2·15	1·28	2·37	1·83	1·85	1·92	2·95	1·91	5·64	5·30	2·39	1·12	2·91	2·72	2·28	0·73	0·94	1·09	1·51	1·90	1·83
Yb	1·84	1·71	2·63	2·47	2·65	3·39	3·48	8·02	3·80	7·82	6·80	8·02	8·03	11·26	6·84	20·50	18·50	8·01	3·41	11·90	11·12	9·51	1·78	2·05	2·96	4·23	5·80	6·10
Lu	0·28	0·25	0·33	0·34	0·39	0·52	0·50	1·19	0·54	1·12	1·00	1·14	1·17	1·59	1·02	2·83	2·53	1·18	0·51	1·76	1·62	1·34	0·26	0·28	0·39	0·59	0·85	0·88
Hf	6·00	5·83	8·12	6·70	5·85	9·20	9·50	24·90	12·81	20·60	22·50	27·90	25·20	36·95	19·70	57·15	52·50	23·30	7·36	40·45	41·20	32·45	3·60	5·91	6·17	8·07	14·29	14·72
Ta	4·30	3·87	6·57	5·20	3·51	6·30	6·50	15·00	8·15	12·80	15·88	17·20	16·90	21·75	10·30	34·80	27·30	11·05	4·36	24·20	23·90	18·55	1·58	3·48	3·64	6·54	8·34	8·01
Pb	7	8	11	6	4	7	9	20	15	7	10	20	12	27	25	95	29	32	30	26	42	12	4	7	6	4	9	4
Th	5·1	5	7·9	7·5	5·9	8·9	8·7	31·6	12·9	17·8	35·4	41·0	35·7	42·8	28·2	110·4	86·8	29·5	8·1	47·7	100·3	49·2	1·7	4·1	4·5	7·5	11·9	11·3
U	1·5	1·5	2·5	2·2	7·1	2·9	1·7	3·2	3·5	4·5	2·0	12·0	10·3	12·7	8·6	33·4	23·7	8·7	4·2	14·5	10·7	13·0	0·5	1·1	1·2	2·1	2·8	3·1

Major elements are given in wt %, trace elements in p.p.m. LOI, loss on ignition; *mg*-number = atomic % $Mg/(Mg+Fe^{2+})$, where Fe^{2+} is calculated using $FeO = 0{\cdot}9(Fe_2O_3)$. bf, black pyroclastic fall; akb, alkali basalt; haw, hawaiite; phntph, phonotephrite; rhy, rhyolite; others as in previous tables. Sample group refers to rock subdivisions based on stratigraphy and chemical characteristics (refer to text).

Table 4: Isotopic analyses of Mt Sidley volcanic rocks and selected samples from Mt Waesche

Sample	Type/stage	Age*	Sm†	Nd†	$^{147}Sm/^{144}Nd$	$^{143}Nd/^{144}Ndm$	$^{143}Nd/^{144}Ndi$	1σ	eps Nd	Rb‡	Sr	$^{87}Rb/^{86}Sr$	$^{87}Sr/^{86}Sr_m$	$^{87}Sr/^{86}Sr_i$	1σ	$\delta^{18}O$§
Mt Sidley																
MB27.5	bas/IV	4·2	7·66	39·08	0·1185	0·512901	0·512898	6	5·1	32	877	0·1055	0·702994	0·702988	7	5·2
	duplicate	4·2	7·74	39·49	0·1185	0·512899	0·512896	3	5·1	32	877	0·1055	0·703000	0·702994	7	-
K168	bas/IV	4·18	7·76	39·80	0·1179	0·512896	0·512893	9	5·0	36	877	0·1187	0·703038	0·703031	10	5·7
MB32.11	DPM/III	4·3	7·44	38·13	0·1179	0·512851	0·512848	4	4·2	40	492	0·2351	0·703165	0·703151	9	1·8
K99	SFM/III	4·3	—	—	—	—	—	—	—	56	756	0·2142	0·703055	0·703042	7	6·2
K134	ben/III	4·3	—	—	—	—	—	—	—	74·70	483·46	0·4468	0·703078	0·703051	7	6·2
K97	ben/III	4·3	11·19	69·14	0·0979	0·512866	0·512863	8	4·5	76·10	490·71	0·4485	0·703016	0·702989	6	5·7
K54	*N*-trac(ui)/III	4·37	—	—	—	—	—	—	—	—	—	—	—	—	—	–1·0
K137	*N*-trac(wf)/III	4·25	—	—	—	—	—	—	—	218·40	3·81	166·1717	0·714708	0·704679	76	5·3
MB29.4	*LT*-trac/II	4·53	12·53	66·43	0·1140	0·512879	0·512876	7	4·7	163·04	7·23	65·2317	0·709201	0·705005	21	5·8
K105	*LT*-trac/II	4·55	—	—	—	—	—	—	—	291·99	36·88	22·9018	0·704768	0·703288	16	4·1
K55	*LT*-trac/II	4·6	13·78	76·08	0·1095	0·512835	0·512832	8	3·9	191·76	195·54	2·8360	0·703337	0·703152	7	5·8
K66	*LT*-trac/II	4·6	10·23	53·12	0·1164	0·512824	0·512820	6	3·6	124·32	78·30	4·5917	0·704119	0·703819	7	7·6
K63A	*LT*- (host)/II	4·6	16·91	90·60	0·1128	0·512810	0·512807	6	3·4	231·16	20·62	32·4200	0·705202	0·703084	20	5·4
K63B	*LT*- (incl)/II	4·6	7·89	40·37	0·1182	0·512833	0·512829	8	3·8	88·10	163·46	1·5586	0·703201	0·703099	7	5·8
MB33.3	*HT*-trac/II	4·58	33·01	183·18	0·1089	0·512813	0·512810	7	3·4	—	—	—	—	—	—	5·4
MB33.8	*HT*-trac/II	4·6	34·51	189·94	0·1098	0·512806	0·512803	3	3·3	—	—	—	—	—	—	5·1
MB35.5	phn (bf)/II	4·7	—	—	—	—	—	—	—	252·80	4·20	174·2270	0·715455	0·703826	94	5·3
MB38.3	trac-phn(bf)/II	4·7	15·23	84·42	0·1090	0·512816	0·512813	8	3·5	266·95	41·84	18·4542	0·705332	0·704100	12	—
MB33.11	trac (bf)/II	4·7	—	—	—	—	—	—	—	372·02	72·99	14·7405	0·704083	0·703099	11	—
MB42.3	phn/I (Sv)	5·08	13·09	74·46	0·1063	0·512859	0·512855	6	4·3	192·48	245·03	2·2716	0·703124	0·702960	8	2·4
K144	phn/I (Sv)	5·0	12·62	70·72	0·1078	0·512882	0·512879	9	4·8	207·92	150·87	3·9853	0·703140	0·702868	8	5·7
K115	phn/I (Sv)	5·0	—	—	—	—	—	—	—	205·71	153·94	3·8644	0·703107	0·702833	7	6·2
MB35.2	phn/I (Sv)	5·0	18·71	102·75	0·1101	0·512863	0·512859	4	4·4	234·65	47·96	14·1505	0·704044	0·703039	11	5·2
K108	tphn/I (Bv)	5·53	17·06	89·40	0·1154	0·512886	0·512882	7	4·9	98·83	194·77	1·4673	0·703052	0·702937	7	3·1
K122	tphn/I (Bv)	5·6	—	—	—	—	—	—	—	105·89	279·99	1·0936	0·703019	0·702932	7	3·8
K137an	anorthoclase	4·25				—				90·71	9·80	26·7780	0·705248	0·703632	15	7·8
MB29.4an	anorthoclase	4·53				—				69·35	12·86	15·5967	0·705210	0·704207	15	8·4
MB35.5an	anorthoclase	4·7				—				100·08	11·10	26·0831	0·705020	0·703279	15	6·5
MB42.3an	anorthoclase	5·08				—				21·89	788·33	0·0803	0·702948	0·702942	7	6·1
K105an	anorthoclase	4·55				—				—	—	—	—	—	—	5·1
MB33.3an	anorthoclase	4·58				—				—	—	—	—	—	—	6·6
K54an	anorthoclase	4·37				—				—	—	—	—	—	—	6·0
Mt Waesche																
MB.4.1	akb	0·1	—	—	—	—	—	—	—	11	494	0·0644	0·702681	0·702681	7	—
K19	akb	0·5	7·33	37·49	0·1182	0·512877	0·512876	9	4·6	25	581	0·1244	0·702732	0·702731	6	—
K01	phntph	0·1	11·18	59·48	0·1137	0·512886	0·512885	8	4·8	51	589	0·2504	0·702697	0·702697	7	—
MB.11.2	tphn	0·5	13·05	68·61	0·1150	0·512890	0·512890	9	4·9	90	201	1·2948	0·702728	0·702719	7	—
MB.15.1	trac	0·5	—	—	—	—	—	—	—	80	221	1·0468	0·702760	0·702753	7	—

akb, alkali basalt; bas, basanite; phntph, phonotephrite; ben, benmoreite; tphn, tephriphonolite; phn, phonolite; trac, trachyte; DPM and SFM, Doumani Peak and south flank mugearites, respectively. ui, unwelded ignimbrite pumice; wf, welded fall; bf, black pyroclastic fall; Sv, Sidley volcano; Bv, Byrd volcano; K63A and B, commingled lava host and inclusion samples. See section on Trachyte Series for definition of *N*-, *LT*- and *HT*-trachyte subdivisions.

*In millions of years (Ma); Mt Sidley $^{40}Ar/^{39}Ar$ determinations from Panter *et al.* (1994), single decimal values indicate interpolated ages.

†Sm and Nd concentrations (p.p.m.) determined by isotope dilution.

‡Rb and Sr concentrations (p.p.m.) determined by XRF and isotope dilution (two significant figures).

§$\delta^{18}O$ values in per mil (‰).

by cup efficiency changes) was normalized using NBS987 to a preferred value of 0·710230. During the present work, BCR-1 gave an $^{87}Sr/^{86}Sr$ value of $0·704991 \pm 14$ ($n=2$) and JB-1 gave $0·704111 \pm 32$ ($n=5$). These results show that JB-1 is not homogeneous.

Lead isotopes were measured using a multicollector VG Sector TIMS (Mukasa *et al.*, 1991). A procedural blank had 0·2 ng of Pb. Precision on the Pb ratios is better than 0·05% at the 95% confidence level, although replicate analyses of NIST standard NBS-981 required applying a fractionation factor of 0·102 per a.m.u.

Oxygen isotopes (Table 4) were measured at New Mexico Tech using a Finnigan MAT delta-E mass spectrometer. $\delta^{18}O$ values are reported in the ‰ notation relative to Vienna Standard Mean Ocean Water (VSMOW; Coplen, 1994). Analyses of quartz standard NBS-28 and an in-house basalt standard gave an analytical precision of $\pm 0·3$‰.

Major element chemistry

Rocks at Mt Sidley are dominated by strongly silica-undersaturated sodic lavas, ranging from basanite to anorthoclase phonolite and comenditic trachyte (Fig. 3). Trachytic lavas and tephra are under- and oversaturated. Some phonolites and trachytes are weakly peralkaline [molecular $(Na_2O + K_2O)/Al_2O_3 \leq 1·2$]. Samples display a decrease in FeO_t, MgO, CaO and P_2O_5 with increasing silica concentration (Fig. 4). The phonolites have restricted SiO_2 between 56 and 58 wt %, whereas trachytes range from 60 to 70 wt % SiO_2. Nevertheless, phonolitic samples display nearly as much variation with respect to other oxides as do the trachytes. The phonolites have higher Al_2O_3 contents (18–21 wt %), whereas the trachytes show lower Al_2O_3 (18–13 wt %) with increasing silica concentration (Fig. 4).

The basanites are not primary mantle melts according to the criteria of Frey *et al.* (1978). The most primitive basanites have *mg*-numbers <56, Ni and Cr <150 p.p.m. (Table 3), olivine of ~Fo_{74}, and trend towards lower CaO and MgO with increasing SiO_2 (Fig. 4), indicating differentiated magmas. Using K_D [(Fe/Mg)/(ol/liq)] = 0·30 at 1 bar (Roeder & Emslie, 1970; Ulmer, 1989), only the cores of olivine phenocrysts (~Fo_{86}) within mafic inclusions of commingled lavas approach equilibrium with primary partial melts from upper-mantle peridotites (calculated *mg*-number ~65 for the coexisting liquid); yet the mafic inclusions in trachyte are unsuitable for use as parental material in fractionation models because of their 'evolved' bulk chemistry (e.g. sample K63b, Table 3).

Mugearites are subdivided into lavas with low *mg*-numbers (20–30) and high P_2O_5 concentrations (>0·9 wt %) restricted to the southern flanks of Mt Sidley (SFM), and tephras with higher *mg*-number (40–50) and moderate P_2O_5 contents (~0·4 wt %) found at Doumani Peak (DPM; Fig. 4). Differences between the two mugearites are small but important for understanding the petrogenetic differences between the trachyte and phonolite suites.

Trace element chemistry

Mt Sidley volcanic rocks have high concentrations of incompatible elements and are enriched in light rare earth elements (LREE) over heavy rare earth elements (HREE) [$(La/Yb)_n = 9–19$], a feature typical of intraplate alkaline magmas. Phonolitic lavas have lower LILE (large-ion lithophile elements)/Zr and LREE/Zr ratios and higher HFSE (high-field strength elements)/Zr ratios relative to trachytic samples. Several trachytes contain ~70 wt % SiO_2 and ≤15% normative quartz, and exhibit extreme incompatible element enrichment (e.g. MB33.8, Table 3; Zr/Rb = 3·5, Zr/Th = 20·0, Zr/La = 7·1 and Zr/Ce = 3·8).

The phonolite lavas have uniform trace element compositions (Fig. 5), considering they were erupted during a ~1 m.y. time-interval from three centers (Panter *et al.*, 1994). The tephriphonolites have similar concentration levels but are less depleted in Ba, K, Sr, P and Ti (Fig. 5b) and they lack significant negative Eu anomalies (Fig. 5a; Eu/Eu*~0·95). The trachytes, in contrast, show a wider range of trace element concentrations, including stronger depletions in Sr, Eu and Ba relative to other compositions.

The least evolved basanites have trace element abundances similar to HIMU (high U/Pb)-type ocean island basalts (OIB). Mt Sidley basanites have lower LILE/HFSE and LREE/HFSE ratios (e.g. sample K109, Table 3; La/Nb = 0·68, Ba/Nb = 5·7, Ba/Th = 68, Th/Nb = 0·085) compared with average EM-type OIB (La/Nb = 0·95, Ba/Nb = 12·8, Ba/Th = 101, Th/Nb = 0·123) (Weaver, 1991) and strong positive Ta and Nb anomalies, relative to LILE and LREE, on primordial-mantle normalized trace element plots (Wood *et al.*, 1981), which is characteristic of HIMU-OIB.

The SFM mugearites have higher elemental abundances and are more LREE enriched [$(La/Yb)_n = 15·5–17$] relative to DPM mugearites [$(La/Yb)_n = 11·5–13$] (Fig. 5c and d). REE levels in DPM rocks are identical to those in less evolved basanites, whereas SFM lavas have REE levels slightly higher than those of the more evolved basanites (Fig. 5c). Alkaline magmas are typically depleted in K relative to Th and Nb on chondrite-normalized diagrams, yet DPM, as well as some trachytes, display flat to small positive K anomalies (Fig. 5b).

Isotope geochemistry

Initial isotopic ratios (Table 4) have been calculated using the $^{40}Ar/^{39}Ar$ dates given by Panter *et al.* (1994). Many

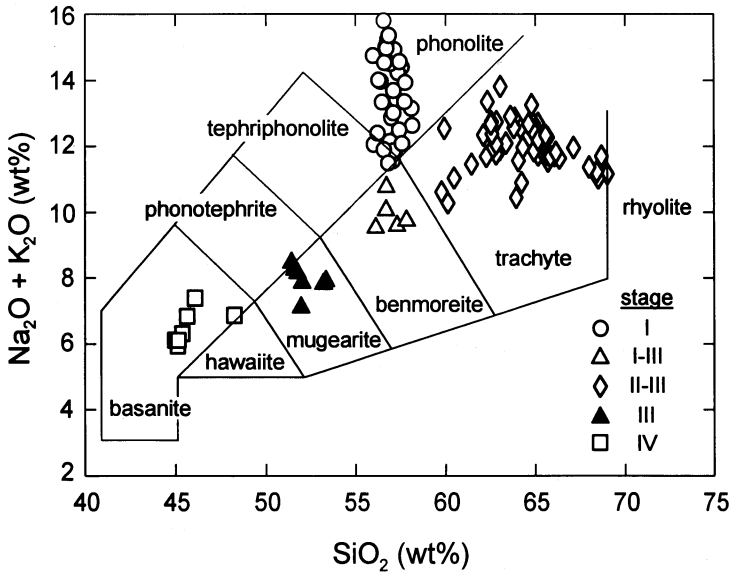

Fig. 3. Classification of Mt Sidley rocks after Le Bas *et al.* (1986).

trachytes and phonolites have high $^{87}Rb/^{86}Sr$ ratios (>10) and hence large corrections in initial $^{87}Sr/^{86}Sr$ ratios (e.g. tephra samples MB35.5 and K137, Table 4). Improved resolution on Sr-poor samples was obtained using anorthoclase separates.

Most samples display a narrow range in $^{87}Sr/^{86}Sr_i$ (0·7028-0·7032), $^{143}Nd/^{144}Nd_i$ (0·51285-0·51290) and $\delta^{18}O$ (5·0-6·0‰), indicating derivation from primitive mantle broadly similar to OIB. Basaltic samples, MB32.11 and MB27.5, have average Pb isotope ratios of $^{206}Pb/^{204}Pb = 19{\cdot}53$, $^{207}Pb/^{204}Pb = 15{\cdot}66$ and $^{208}Pb/^{204}Pb = 39{\cdot}14$ (Panter, 1995), indicating a significant HIMU mantle component (Zindler & Hart, 1986), consistent with trace element data. Initial Sr–Nd isotope data for Mt Sidley and Mt Waesche plot just below the HIMU mantle field (Fig. 6) defined by Mangaia Island samples (Woodhead, 1996). A HIMU-OIB isotopic component ($^{87}Sr/^{86}Sr \leq 0{\cdot}703$ and $^{206}Pb/^{204}Pb \geq 19{\cdot}5$) is ubiquitous in Late Cenozoic volcanic rocks throughout west Antarctica (Kyle *et al.*, 1992, 1994; Hart & Kyle, 1994) and suggests a common mantle reservoir for west Antarctic rift volcanism (Hart *et al.*, 1994; Hole & LeMasurier, 1994; Weaver *et al.*, 1994).

The variation of $^{143}Nd/^{144}Nd_i$ with $^{87}Sr/^{86}Sr_i$ (Fig. 6) is explained by interaction of a HIMU-OIB source with crust. For the majority of samples, as Nd becomes less radiogenic (from ~0·51290 to 0·51280), $\delta^{18}O$ remains between 5·5 and 6·5‰, and $^{87}Sr/^{86}Sr_i$ varies from ~0·7028 to 0·7032. This may indicate a contaminant characterized by a relatively low time-integrated Rb/Sr signature. The decrease in radiogenic Nd broadly correlates with sample differentiation and increasing LREE, HFSE and Rb/Sr ratios from basanite (e.g. 0·512898 for sample MB27.5) to trachyte (e.g. 0·512803 for sample MB33.8) compositions. A notable exception is mugearite sample MB32.11 (DPM type), which has trace element abundances similar to those of primitive basanite (Fig. 5c and d) but possesses a lower $^{143}Nd/^{144}Nd_i$ value (0·512848). Several highly differentiated samples (mainly trachytes) have high $^{87}Sr/^{86}Sr_i$ (0·7033–0·7042), low $^{143}Nd/^{144}Nd_i$ (0·51281–0·51283) and elevated $\delta^{18}O$ (6·5–8·4 ‰) values (Table 4). A positive correlation of increasing $\delta^{18}O$ with $^{87}Sr/^{86}Sr_i$ (Fig. 7) offers strong support for assimilation of crust by mantle-derived magmas (see James, 1981).

Twelve of the 32 samples analyzed for oxygen isotopes display $\delta^{18}O$ values of $\leq 4{\cdot}0$‰. The extent of ^{18}O depletion shows a positive correlation with LOI. There is also a broad correlation between high-LOI, low-$\delta^{18}O$ values and incipient alteration (palagonitized glass and amygdaloidal zeolites and calcite). The low $\delta^{8}O$ samples are considered to be the result of low-temperature hydration and exchange with extremely light ($\delta^{18}O < -30$‰) Antarctic meteoric waters. Water–rock interaction is restricted to the alteration of available glass and secondary mineralization by solution-precipitation within vesicles, voids and fractures. Anorthoclase phenocrysts appear to be unaffected by alteration-exchange and contain consistently higher, magmatic, $\delta^{18}O$ values relative to whole-rock values (Table 4 and Fig. 7). Apart from minor leaching of alkali metals in some phonolites, other elements, including Ba, appear to be unaffected by surficial alteration at Mt Sidley.

In Fig. 7, anorthoclase phenocrysts from three pyroclastic tephra deposits (samples MB35.5, K137 and MB29.4) have lower Sr isotope ratios and higher $\delta^{18}O$

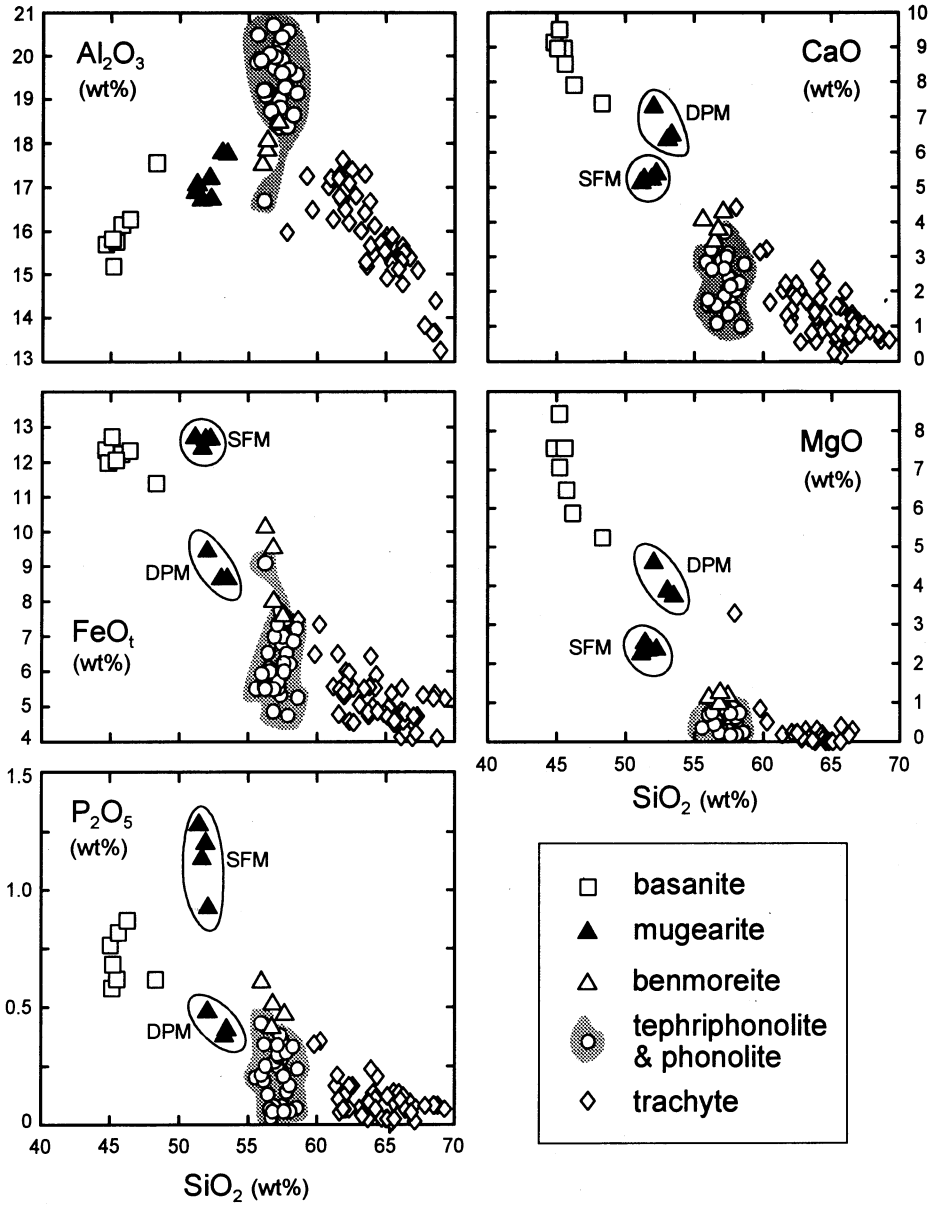

Fig. 4. Variation of selected major elements with silica content. Mugearites are subdivided into two types: low MgO, high FeO_t and P_2O_5 lavas located on Mt Sidley's southern flank (SFM); and higher MgO and CaO tephra from Doumani Peak (DPM).

values relative to the whole rocks from which they were separated. This difference can be explained in three steps by a combination of primary and secondary processes (inset Fig. 7).

MAGMA GENESIS

On the basis of geological mapping and stratigraphy (Panter *et al.*, 1994), the phonolites and trachytes cannot be related by evolution in a simple magma system. Moreover, major and trace element data indicate separate magmatic lineages for trachytic and phonolitic compositions.

Magma genesis by fractional crystallization is evaluated by the least-squares mass balance methods using major elements (Table 3) and phenocryst chemistry [Tables 2 and 3; other analyses taken from Panter (1995)]. Mass balance models are further tested through trace element approximations using published mineral–liquid partition coefficients (K_D values) determined for alkaline assemblages (Table 5) and the Rayleigh fractionation

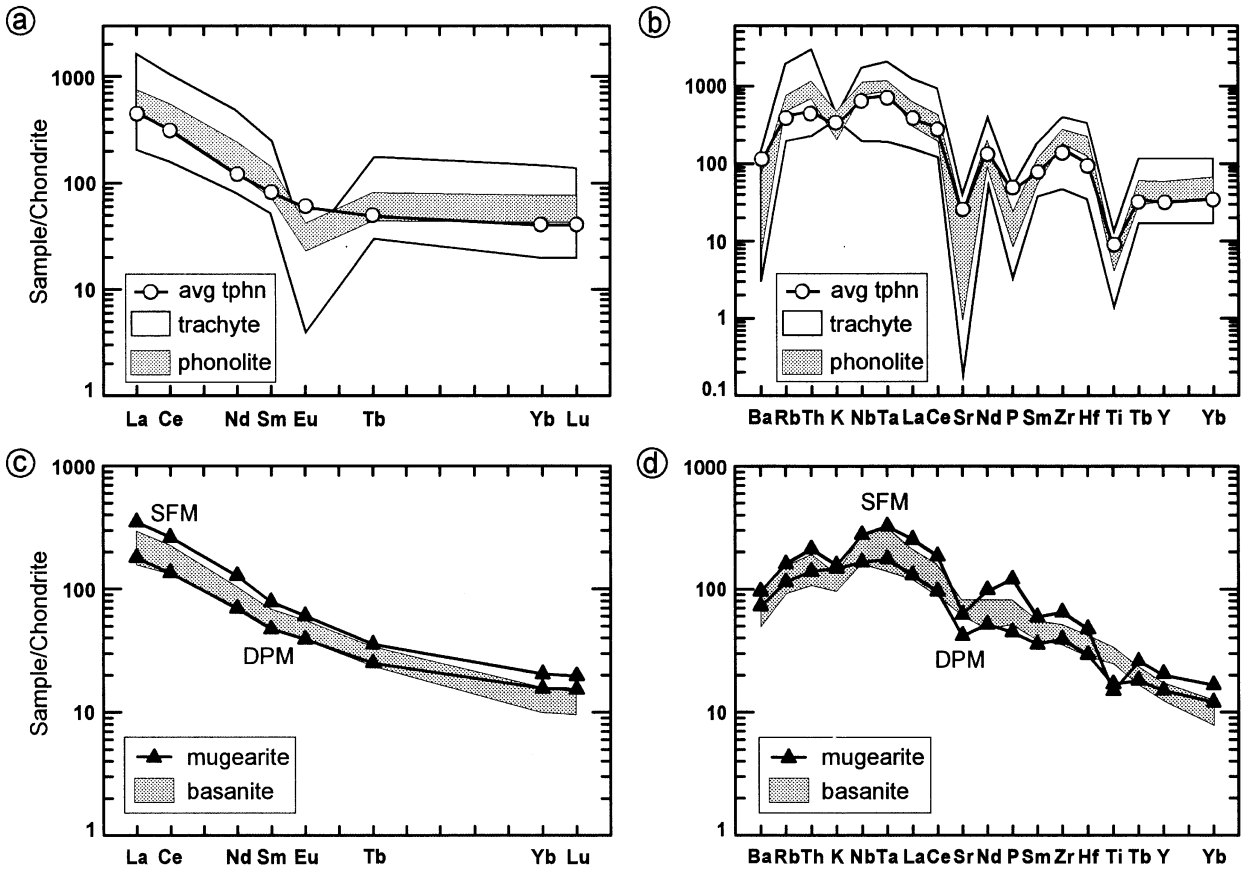

Fig. 5. Chondrite-normalized REE and trace element patterns of representative Mt Sidley rocks, using normalizing values of Sun & McDonough (1989) and Thompson *et al.* (1984), respectively.

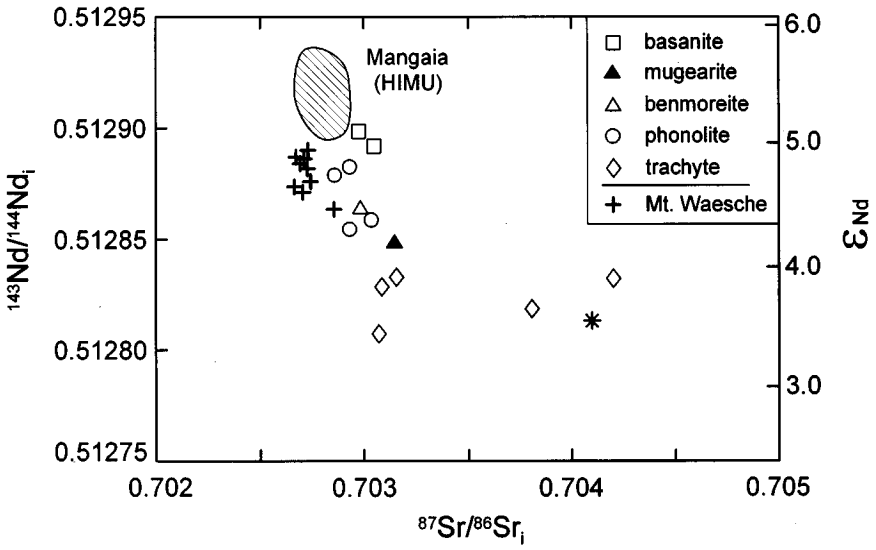

Fig. 6. Age corrected Sr–Nd isotope plot. The shaded field encompasses data from Mangaia Island (Woodhead, 1996). Asterisk represents a black, compositionally heterogeneous (phonolite–trachyte), pyroclastic fall deposit marking the transition between stage I and stage II activity.

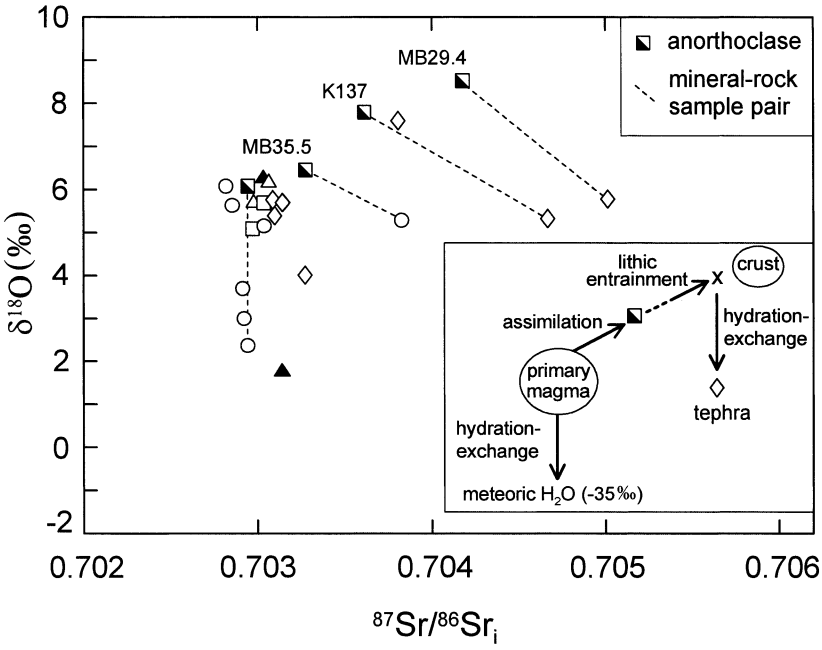

Fig. 7. $\delta^{18}O$ vs initial $^{87}Sr/^{86}Sr$. Half-shaded squares represent anorthoclase and other symbols are for whole-rock compositions (as in previous diagrams). Dashed lines connect anorthoclase to whole rocks from which they were separated. Two general trends are observed: (1) a positive correlation between O and Sr isotopes, reflecting assimilation of crust by magmas; (2) a trend towards lower $\delta^{18}O$ values (<5‰), indicating hydration-exchange between glass and Antarctic meteoric waters (–35‰). Anorthoclase separated from three pyroclastic tephras (samples MB35.5, K137 and MB29.4) has lower Sr isotope ratios and higher $\delta^{18}O$ values relative to whole rocks. To explain the discordance, a three-stage process is envisaged (see inset): (1) assimilation of crust by magmas produced the isotopic signature recorded by anorthoclase (shaded square); (2) physical entrainment of crust by erupting magmas resulted in bulk analyses (lithics + pumice + matrix) with $^{87}Sr/^{86}Sr$ and $\delta^{18}O$ above magmatic values (×); (3) alteration of lithic-rich tephras by meteoric water produced the isotopic signature of bulk analyses (open diamond).

equation (Arth, 1976). It is important to emphasize that basanites and mugearites are younger than phonolites and most trachytes (Panter *et al.*, 1994) but they are assumed to be representative of parental magmas. In addition, rock compositions from the younger Mt Waesche volcano are used to model some aspects of Mt Sidley petrogenesis.

Bulk distribution coefficient (*D*) values were also determined by regression of trace element data on log–log diagrams [method of Allègre *et al.* (1977); after Treuil & Joron (1975)], using Th as a reference incompatible element ($D^{Th} \ll 1$) (Table 6). In general, data regressed for Ba, Sr, Eu and K show low correlation coefficients (Table 6), and the scatter on log–log plots may reflect changes in feldspar stoichiometry. In addition, poor correlation of data on log–log diagrams for several rock suites does not allow *D* to be determined.

Phonolite series

Basanite sample K109 (Table 3) is considered representative of the parental magma for the phonolite series. Basanitic scoria cones at Mt Sidley contain lower-crustal and upper-mantle xenoliths. Wysoczanski (1993) described the xenoliths as being angular in form and devoid of decompressive melting textures, attesting to their rapid entrainment and ascent to the surface. This suggests that basanitic melts differentiated within the upper mantle or near the base of the crust (~30–35 km; Wysoczanski, 1993).

Fractional crystallization

Fractional crystallization (FC) models predict two fractionation schemes for the phonolite series: a high-alkali trend evolving tephriphonolites and phonolites from basanite (phonolitic sequence, Tables 7 and 8, models A–E); and an intermediate sequence producing mugearite and benmoreite liquids from basanite (models F–H in Tables 7 and 8). Differentiation of basanite by fractionation of diopside, olivine, plagioclase, titaniferous magnetite, nepheline and/or apatite produces ~35% mugearite (models F and G), 25% benmoreite (models F–H), and ~20% tephriphonolite and phonolite liquids (models A–C).

The compositions of phonolitic lavas within the high alkali trend are distinct for each stage I volcano and together show a compositional continuum (Fig. 8a). Although the order is inconsistent with the observed stratigraphy, the trend emulates progressive differentiation

Table 5: Published mineral–melt partition coefficient (K_D) values

	Plagioclase ~An_{65}		Plagioclase ~An_{40}		Clinopyroxene			Olivine	Magnetite		Alkali feldspar		Amphibole	Nepheline	Apatite	
	MA-6	HPP	MA-10	HPP	MA-2	MA-4	HPP	MA-3	MA-7	MA-5	MA-12	HPP	MA-11	GIP	MA-8	HPP
Sc	0·02	—	0·03	—	2·39	2·65	—	0·20	5·04	1·39	0·22	—	7·58	—	0·41	—
Rb	0·03	—	0·20	—	0·10	0·04	—	0·08	0·23	0·08	0·42	—	0·15	0·44	0·56	—
Sr	2·12	1·36	4·41	4·62	0·33	0·16	1·51	—	0·23	0·16	4·11	5·57	1·01	0·24	1·67	0·83
Ba	0·24	0·15	1·08–4·65	1·47	0·07	0·04	0·321	0·04	0·14	0·14	3·02	5·04	0·61	0·09	0·95	0·014
La	0·12	0·023	0·46	0·28	0·22	0·10	0·10	0·02	0·53	0·20	0·46	0·219	0·56	0·01	5·16	15·20
Ce	0·14	0·023	0·36	0·215	0·34	0·20	0·18	—	0·56	0·20	0·36	0·173	0·87	0·011	6·34	16·60
Nd	0·07	0·023	0·31	0·170	0·68	0·60	0·38	—	0·55	0·20	0·31	0·152	1·82	0·013	6·60	21·00
Sm	0·12	0·024	0·27	0·135	0·66	0·60	0·56	—	0·55	0·20	0·27	0·139	2·40	0·012	6·30	20·70
Eu	0·22	0·232	1·78	1·10	0·65	0·57	0·58	0·03	0·15	0·06	1·78	1·72	2·08	0·043	3·77	14·5
Tb	0·03	0·018	0·23	0·111	0·77	0·70	0·73	0·04	0·55	0·19	0·23	0·130	2·88	0·014	5·79	19·8
Yb	0·11	0·030	0·18	0·062	0·73	0·70	0·61	—	0·75	0·20	0·18	0·116	1·77	0·016	3·24	9·4
Lu	0·18	—	0·11	—	0·73	0·70	—	—	0·75	0·20	0·11	—	1·77	—	3·40	—
Hf	0·01	—	0·15	—	0·69	0·43	—	0·05	1·77	0·24	0·13	—	0·80	0·008	0·64	—
Ta	0·01	—	0·08	—	0·14	0·04	—	0·03	3·86	0·39	0·12	—	0·89	—	0·09	—
Th	0·02	—	0·16	—	0·13	0·03	—	0·04	0·53	0·18	0·13	—	0·09	0·014	0·95	—

Sources of K_D data: MA, Mururoa Atoll (Caroff *et al.*, 1993); HPP, Hut Point Peninsula (Kyle, 1981); GIP, Gardar Igneous Province (Larsen, 1979).

*Table 6: Bulk distribution coefficients (*D*) calculated from log–log diagrams*

	Basanite	R^2	Tephriphonolite	R^2	*N*-trachyte	R^2
Sc	1·66	0·78	*P*>1	0·64	3·64	0·66
Rb	0·03	0·87	—	—	0·27	0·92
Sr	—	—	1·92	0·88	3·74	0·68
Ba	0·29	0·43	—	—	—	—
La	0·12	0·84	0·79	0·93	0·15	0·94
Ce	0·18	0·78	1·30	0·97	0·09	0·95
Nd	0·31	0·69	0·67	—	0·25	0·83
Sm	0·49	0·47	0·54	0·92	0·24	0·84
Eu	0·74	—	0·73	0·47	2·14	0·39
Tb	0·36	0·90	0·45	0·84	0·15	0·84
Yb	0·19	0·93	0·03	0·99	0·12	0·97
Lu	0·34	0·81	0·19	0·92	0·19	0·93
Hf	0·45	0·80	0·74	0·50	0·02	0·98
Ta	0·12	0·87	—	—	0·08	0·96
Y	0·44	0·83	0·08	0·96	0·09	0·93
Zr	0·37	0·96	0·47	0·63	0·01	0·94
Nb	0·17	0·80	0·83	0·74	0·06	0·96
K	0·55	0·70	1·22	0·42	—	—

Slope $P=(1-D^i)$. Dashes indicate uncorrelatable data.

of Byrd magmas through Sidley compositions to Weiss phonolites. If a common lineage is assumed, strong depletions in Ba (Fig. 8) must reflect substantial loss of alkali feldspar, which is underscored by an overall decrease in its average modal abundance between Byrd (33%), Sidley (13%) and Weiss (5%) lavas. Fractional crystallization models offer good estimates for the evolution of tephriphonolite to phonolite (Tables 7 and 8, model E); however, for the majority of Sidley volcano phonolites, FC models give poor solutions (Fig. 8b–d). It is considered unlikely that the compositional variations in the phonolites of the Sidley volcano reflect a simple liquid line of descent.

The feldspar phyric character of the phonolites suggests cumulus enrichment and the analyses of highly porphyritic lavas may deviate from normal liquid lines of descent (Cox *et al.*, 1979). The phonolites of the Sidley volcano, which plot above model fractional crystallization curves in Fig. 8b–d, show a relative enrichment in elements compatible with feldspar addition (K, Ba, Sr and Eu). They are also enriched in several incompatible elements (Ta, Hf and Th) with respect to model liquids (Fig. 8c); this feature could reflect chemical enhancement by glass and mineral inclusions (e.g. apatite) observed within large phenocrysts. However, feldspar accumulation should show Eu anomalies on chondrite-normalized trace element diagrams, but in fact, all phonolites show strong relative depletions in Eu, Ba, K and Sr, indicating feldspar fractionation (Fig. 5a and b).

Magma mixing

We interpret the chemical departure of phonolites from FC model liquids to result from mixing between magmas from the phonolite series. Mixing is consistent with reverse zoning in olivine, clinopyroxene and feldspar phenocrysts and crystal–liquid disequilibrium within the stage I Sidley volcano sequence. Similar disequilibrium textures occur in the inclusion-bearing trachytic lavas of stage II, where strong mafic–felsic magma interaction is explicit. However, unlike the commingled lavas (heterogeneous mixtures) which contain coexisting anorthoclase and forsterite ($Fo_{86–82}$), hybrid phonolites possess a phenocryst assemblage that is considered to be in equilibrium with a limited range of melt compositions. Furthermore, calculated liquid compositions in chemical equilibrium with olivine cores and rims (*mg*-number increases from core to rim) show small, yet statistically significant differences, suggesting that mixing between endmembers of the phonolitic spectrum is likely. Two lavas featuring pronounced disequilibrium textures, samples K144 and K149, plot along with other Sidley volcano phonolites off the FC model curve (Fig. 8b–d).

Table 7: Least-squares mass balance solutions for Phonolite Series rocks

	SiO_2	TiO_2	Al_2O_3	FeO	MnO	MgO	CaO	Na_2O	K_2O	P_2O_5	ΣR^2
Phonolitic sequence											
A	*basanite (K109)→'evolved' basanite (K133)*										
K109 = 0·609(K133) + 0·114Cpx (En_{48}) + 0·061Ol (Fo_{86}) + 0·132Pl (An_{63}) + 0·048Mt (Usp_{65}) + 0·036Ne											
meas.	45·12	3·06	15·18	12·09	0·17	8·43	9·42	4·46	1·46	0·59	
calc.	45·22	3·04	15·11	12·09	0·22	8·42	9·40	4·48	1·36	0·53	0·032
B	*evolved basanite (K133)→phonolite (K149)*										
K133 = 0·326(K149) + 0·125Cpx (En_{48}) + 0·072Ol (Fo_{86}) + 0·268Pl (An_{47}) + 0·129Mt (Usp_{58}) + 0·02Ap + 0·06Ne											
meas.	46·09	3·06	16·18	12·34	0·21	5·87	7·99	5·42	1·97	0·86	
calc.	46·15	3·11	16·12	12·32	0·27	5·86	7·97	5·45	1·91	0·88	0·019
C	*evolved basanite (K133)→tphn-phn (K114)*										
K133 = 0·329(K114) + 0·132Cpx (En_{48}) + 0·067Ol (Fo_{86}) + 0·237Pl (An_{47}) + 0·13Mt (Usp_{58}) + 0·02Ap + 0·085Ne											
meas.	46·09	3·06	16·18	12·34	0·21	5·87	7·99	5·42	1·97	0·86	
calc.	46·17	3·15	16·09	12·31	0·27	5·86	7·96	5·45	1·89	0·89	0·036
D	*tephriphonolite (K122)→'evolved' tephriphonolite (K121)*										
K122 = 0·933(K121) + 0·057Akf (Or_{20}) + 0·001Ap + 0·009Ne											
meas.	57·92	0·79	18·55	6·78	0·23	0·67	2·45	7·63	4·66	0·30	
calc.	57·91	0·79	18·62	6·77	0·24	0·73	2·44	7·61	4·67	0·32	0·010
E	*tphn-phn (K114)→phonolite (MB35.2)*										
K114 = 0·478(MB35.2) + 0·02Ol (Fo_{65}) + 0·223Pl (An_{35}) + 0·199Akf (Or_{48}) + 0·03Mt (Usp_{65}) + 0·01Ap + 0·04N											
meas.	57·13	0·79	19·90	5·95	0·18	0·73	2·76	7·72	4·55	0·28	
calc.	57·20	0·80	19·92	5·95	0·17	0·72	2·67	7·70	4·46	0·38	0·032
Intermediate sequence											
F	*basanite (K109)→evolved basanite (K95)*										
K109 = 0·629(K95) + 0·188Cpx (En_{50}) + 0·055Ol (Fo_{86}) + 0·019Pl (An_{54}) + 0·044Mt (Usp_{65}) + 0·005Ap + 0·06Ne											
meas.	45·12	3·06	15·18	12·09	0·17	8·43	9·42	4·46	1·46	0·59	
calc.	45·21	3·07	15·09	12·08	0·23	8·42	9·41	4·52	1·26	0·60	0·064
G	*evolved basanite (K95)→mugearite (SFM, K93)*										
K95 = 0·558(K93) + 0·070Cpx (En_{48}) + 0·057Ol (Fo_{86}) + 0·226Pl (An_{54}) + 0·050Mt (Usp_{65}) + 0·039Ne											
meas.	48·25	2·51	17·55	11·40	0·19	5·24	7·38	5·22	1·65	0·62	
calc.	48·23	2·44	17·53	11·43	0·20	5·23	7·39	5·27	1·49	0·63	0·035
H	*mugearite (SFM, K93)→benmoreite (K134)*										
K93 = 0·758(K134) + 0·019Cpx (En_{45}) + 0·051Ol (Fo_{65}) + 0·110Pl (An_{54}) + 0·046Mt (Usp_{58}) + 0·016Ap											
meas.	51·58	1·58	17·01	12·45	0·24	2·50	5·25	5·97	2·28	1·14	
calc.	51·57	1·61	17·01	12·44	0·29	2·51	5·25	5·96	2·33	1·13	0·006

Cpx, clinopyroxene; Ol, olivine; Pl, plagioclase; Mt, titaniferous magnetite; Ap, apatite (from Kyle, 1986); Ne, nepheline (from Deer *et al.*, 1966); Akf, alkali feldspar.

On a log Ba vs log Th plot (Fig. 8c), phonolites of the Sidley volcano form a curving array between compositions of the Byrd and Weiss volcanoes. The data can be approximated by modeled mixing hyperbola (Fig. 8c). An origin by magma mixing for Sidley phonolites is further supported by the broad linear correlation with Byrd tephriphonolites shown in Fig. 8d [a companion plot to Fig. 8b; see Langmuir *et al.* (1978)]. The scatter of data about a straight line of mixing may be attributable to crystal fractionation following hybridization and/or multiple mixing events allowing for slight variations in endmember compositions.

Trachyte series

Mt Sidley trachytes form three main types based on stratigraphy, and differences in chemical (Fig. 9) and

Table 8: Elemental concentrations for FC models (Table 7) calculated using published K_D *values (Table 5)*

Phonolitic sequence

	A bas→bas K109 to (0·609)K133		**B** bas→phn K133 to (0·326)K149		**C** bas→tphn K133 to (0·329)K114		**D** tphn→tphn K122 to (0·933)K121		**E** tphn→phn K114 to (0·478)MB35.2	
	meas. 109	calc.	meas. 133	calc.	meas. 133	calc.	meas. 122	calc.	meas. 114	calc.
Sc	21·8	20·6	17·3	4·47	17·3	5·69	3·2	3·12	3·3	0·68
Rb	35	35·55	55	75·60	55	52·63	111	144·19	140	141·05
Sr	752	782·93	950	954·48	950	925·81	313	317·46	322	338·92
Ba	344	432·28	666	679·20	666	757·62	732	748·03	663	528·74
La	40·7	45·58	68·8	82·48	68·8	67·02	103·5	106·49	98·9	110·06
Ce	82·8	91·01	134·0	153·59	134·0	139·76	244·0	216·23	201·7	191·68
Nd	32·0	35·86	51·0	60·01	51·0	50·22	70·0	63·22	60·0	63·09
Sm	7·60	7·96	11·27	11·03	11·27	10·28	13·74	14·28	12·56	11·32
Eu	2·43	2·25	3·20	3·53	3·20	4·01	4·22	4·35	3·36	2·08
Tb	0·96	0·88	1·24	1·53	1·24	1·42	1·85	1·90	1·77	1·68
Yb	1·84	1·90	2·63	4·58	2·63	3·61	5·24	6·66	6·30	6·15
Lu	0·28	0·24	0·33	0·54	0·33	0·44	0·81	1·01	0·94	0·89
Hf	6·00	6·12	8·12	10·99	8·12	9·44	18·70	20·13	21·50	19·88
Ta	4·3	5·18	6·6	6·45	6·6	5·27	12·6	12·68	13·7	12·60
Th	5·1	5·09	7·9	13·77	7·9	8·16	11·7	14·27	21·0	20·43

Intermediate sequence

	F bas→bas K109 to (0·629)K95		**G** bas→mug K95 to (0·558)K93		**H** mug→ben K93 to (0·758)K134	
	meas. 109	calc.	meas. 95	calc.	meas. 93	calc.
Sc	21·8	22·25	15·0	6·42	6·5	3·47
Rb	35	29·95	44	33·32	56	67·35
Sr	752	742·02	715	649·37	734	768·14
Ba	344	289·34	404	405·54	662	783·72
La	40·7	39·57	52·5	49·38	80·6	91·28
Ce	82·8	77·59	99·2	95·94	153·9	159·46
Nd	32·0	33·78	39·0	39·11	62·0	62·06
Sm	7·60	6·72	7·80	7·29	11·42	10·79
Eu	2·43	1·99	2·39	2·12	3·31	3·18
Tb	0·96	0·88	1·00	0·83	1·31	1·19
Yb	1·84	2·04	2·47	2·20	3·39	3·65
Lu	0·28	0·27	0·34	0·34	0·52	0·52
Hf	6·00	5·51	6·70	6·19	9·20	11·05
Ta	4·3	4·20	5·2	4·62	6·3	6·77
Th	5·1	4·72	7·5	5·26	8·9	10·45

bas, basanite; mug, mugearite; ben, benmoreite; tphn, tephriphonolite; phn, phonolite.

lithologic character. With increasing stratigraphic height they are: (1) high-Th (*HT*)-trachyte, lavas and lithic breccias distinguished by Th contents >60 p.p.m. and low K/Nb ratios (<200); (2) low-Th (*LT*)-trachyte, tephras and lavas, including commingled units, which are characterized by having lower overall incompatible element

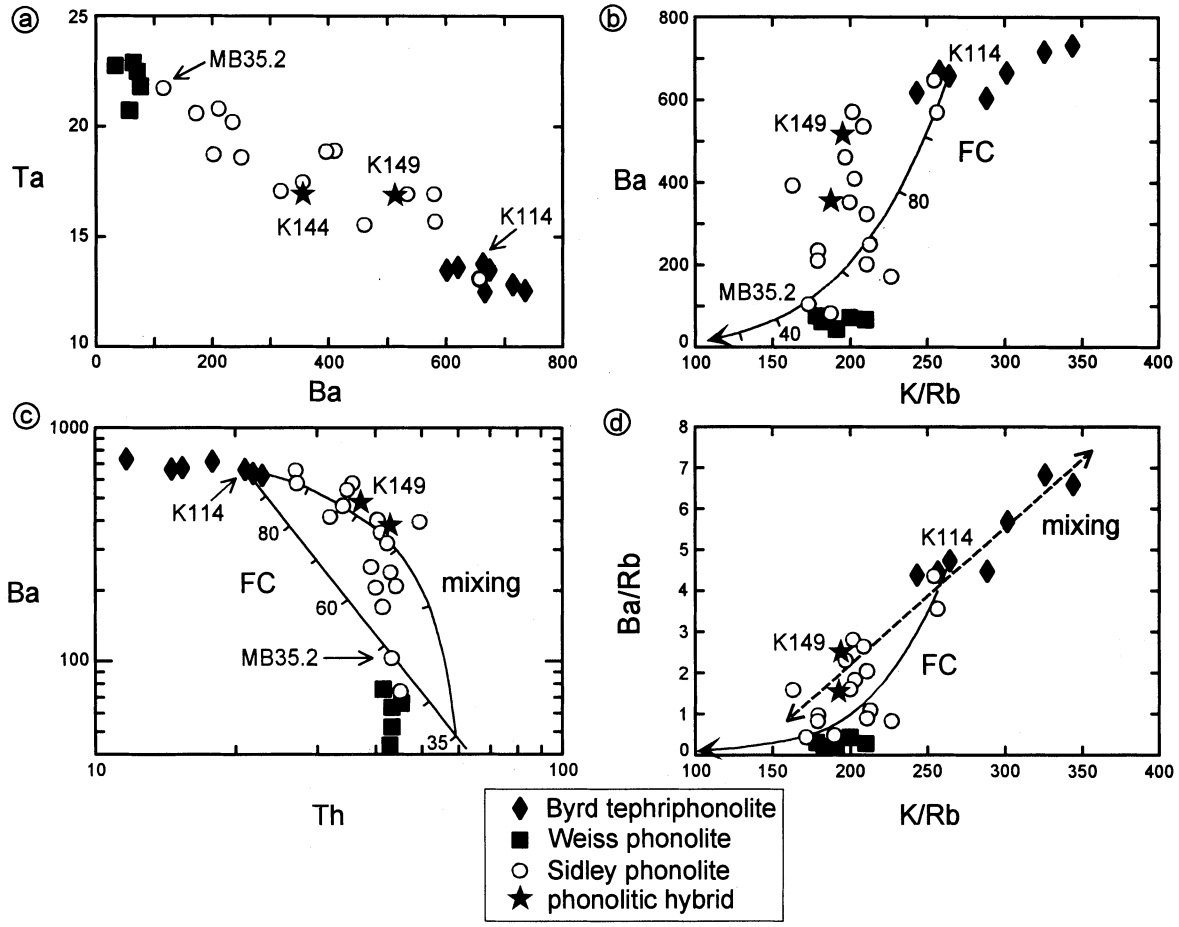

Fig. 8. Trace element (p.p.m.) variations for phonolites of the stage I succession (oldest to youngest: Byrd→Weiss→Sidley volcanoes). Solid stars represent hybrid lavas. (a) Ta vs Ba. Decrease in Ba content is due to fractionation of alkali feldspar. (b) Ba vs K/Rb showing closed system fractional crystallization (FC) of sample K114. Model curve calculated using $D^{K}=0{\cdot}8$, $D^{Rb}=0{\cdot}2$ and $D^{Ba}=3{\cdot}5$ (Table 7, model E). Numbered tick marks indicate the percent magma remaining. (c) Variation of Ba with Th. Fractional crystallization of K114 (straight line) is calculated using $D^{Ba}=3{\cdot}5$ and $D^{Th}=0{\cdot}01$. Mixing sample K114 with a hypothetical composition derived from 65% crystallization of K114 closely approximates hybrid compositions. Tick marks on the mixing hyperbola are in 20% increments. (d) Ba/Rb vs K/Rb (compare with b) showing a linear mixing trend for data plotted above the FC curve (inclusive of hybrid samples).

abundances (Th <50 p.p.m.) and high K/Nb ratios (some >500); (3) 'normal' (*N*)-trachyte, tephras with intermediate incompatible trace element concentrations. Although *N*-trachytes are chemically similar to some 'evolved' (e.g. Th>20 p.p.m.) *LT*-trachytes, they represent a separate magma batch erupted during a single, stage III caldera-forming event (conformable units; welded pyroclastic fall and unwelded ignimbrite) that occurred more than 100 ka after the eruption of the cogenetic *HT*-, *LT*-trachyte sequence.

The evolution of coexisting undersaturated and oversaturated rocks is often bound by the assumption of a common parent. At Mt Sidley, parental magmas which evolved trachytic and phonolitic magmas are distinct, thus providing a fundamental basis for their diverging petrogenesis. The formation of the trachyte series by fractionation of basanite liquids was evaluated using least-squares models and Rayleigh trace element approximations, and produced unsatisfactory results. The inconsistencies of the models do not unequivocally preclude a basanite parent, but may reflect overprinting by open system processes. Still, the temporal and spatial separation of trachytic and phonolitic activity suggests that they developed within discrete systems (Panter *et al.*, 1994), and their evolution from separate parental magmas is investigated below.

The strong geochemical dissimilarity between mugearite types DPM and SFM (Figs 4 and 5c and d) requires the existence of at least two separate basaltic parental compositions. At Mt Sidley only basanites (>10% *ne*) are exposed. Alkali basalts (<8% *ne*) from Mt Waesche are shown with other mafic compositions on a plot of

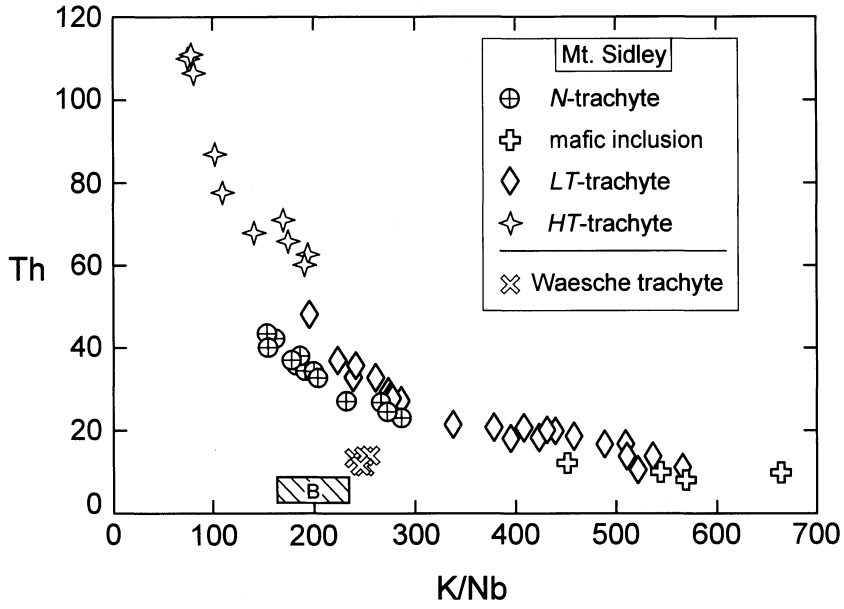

Fig. 9. Th (p.p.m.) vs K/Nb diagram showing main trachyte types: *HT*-trachyte (high-Th, low K/Nb); *LT*-trachyte (low-Th, high K/Nb); *N*-trachyte ('normal' trachytes having intermediate concentrations). Mafic inclusions (open crosses) are hosted by *LT*-trachyte lavas (commingled lavas). Shaded box (B) includes basanite from Mt Sidley and alkali basalt from Mt Waesche.

La/Yb vs *mg*-number in Fig. 10. Values of La/Yb for SFM lavas fall within the range of Sidley basanites but they have significantly lower *mg*-numbers (Fig. 10). Progressive fractionation of olivine, clinopyroxene, plagioclase, magnetite and nepheline from a basanite magma in the proportions predicted by FC models (i.e. Tables 7 and 8, model G) can explain this relationship. On the other hand, DPM samples cannot result from basanite fractionation, as incompatible element concentrations in the former have similar or lower levels (Table 3; Fig. 5c and d). We argue that fractional crystallization of alkali basalt can produce hawaiite and more evolved magmas broadly similar to Mt Sidley DPM and *N*-trachyte compositions. The relationship between alkali basalt and basanite shown in Fig. 10 cannot be explained by fractional crystallization but may reflect source variations; an interpretation supported by their distinctive isotopic characteristics (Fig. 6).

Fractional crystallization of alkali basalt

We propose that DPM-type mugearites and *N*-trachytes represent magmas derived by fractional crystallization of 'Waesche-type' alkali basalts. Incompatible trace elements (e.g. Nb, Zr, Rb and La) for Mt Waesche rocks show extremely good linear correlations ($R^2 \geq 0{\cdot}95$) on log C^{Th} vs log C^{i} diagrams, indicating that differentiation was controlled by fractional crystallization processes. Changes in slope on logarithmic plots (positive to negative) are restricted to elements compatible with feldspars (K, Ba, Sr and Eu) in evolved compositions. A two-step least-squares mass balance model describes the genesis of Waesche trachytes from alkali basalts by fractionation of clinopyroxene, olivine, plagioclase, magnetite and apatite (Table 9). In Table 9, the calculated bulk distribution coefficients decrease slightly with differentiation for all elements except Sr and Eu. Their compatible behavior corresponds to an increase in the modal proportion of plagioclase subtracted for mass balance calculations.

Assessment of crustal contributions

The assimilation of crust by silica-undersaturated mantle-derived melts has been used to explain the genesis of silica-oversaturated trachytes (e.g. Foland *et al.*, 1993; Macdonald *et al.*, 1995), yet silica oversaturation may be explained without additions from the crust. One mechanism involves the removal of silica-poor phases (amphibole or spinel) to promote silica oversaturation of residual liquids (e.g. Fitton, 1987; Cox *et al.*, 1993). Although minor amounts of arfvedsonite exist within some trachytes (Tables 1 and 2) the fractionation of such silica-rich (up to 52 wt % SiO_2), *hy*-normative (~57%), amphiboles could not produce a silica-oversaturated residual.

The high LILE/HFSE ratios for *LT*-trachytes, which distinguish them from other trachytes including those from Mt Waesche (Fig. 9), are interpreted as indicating contribution from a crustal source depleted in HFSE. The depletion in HFSE relative to LREE and LILE is

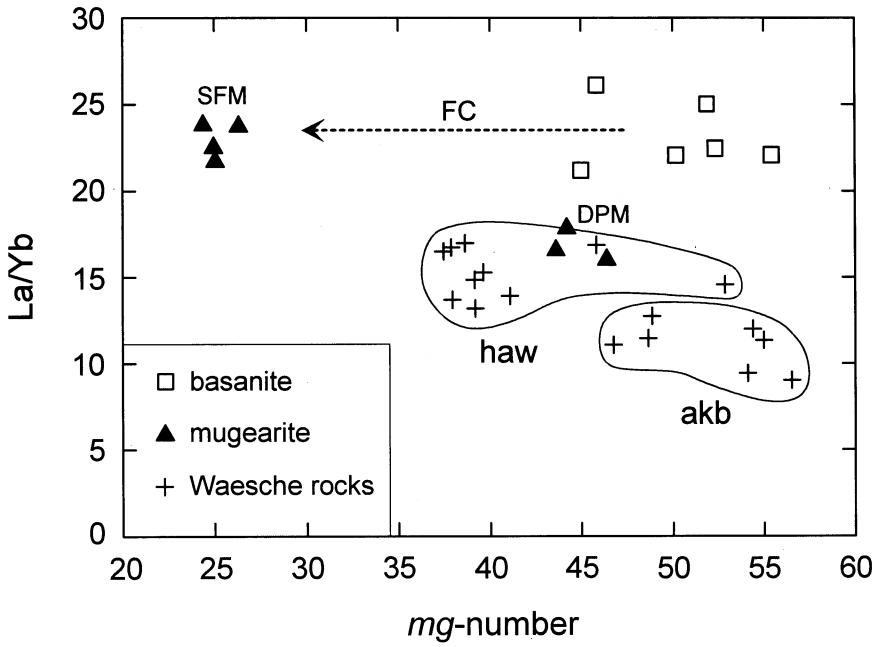

Fig. 10. Plot of La/Yb vs *mg*-number [atomic % = Mg/(Mg + Fe^{2+})] showing mugearite types, DPM and SFM, relative to basanite and Mt Waesche basalts (akb). Dashed arrow represents the general fractional crystallization trend for basanite (model G, Table 7). FC models also predict the evolution of alkali basalt (akb) to hawaiite (haw) for the Mt Waesche suite (Table 9).

Table 9: Least-squares mass balance and Rayleigh fractionation for Mt Waesche rocks

	SiO_2	TiO_2	Al_2O_3	FeO	MnO	MgO	CaO	Na_2O	K_2O	P_2O_5				ΣR^2
alkali basalt (MB4.1)→mugearite (MB21.1)														
MB4.1 = 0·31(MB21.1) + 0·14Cpx (En_{48}) + 0·09Ol (Fo_{86}) + 0·37Pl (An_{61}) + 0·08Mt (Usp_{49}) + 0·01Ap														
meas.	46·35	2·06	16·80	11·32	0·18	7·75	11·09	3·36	0·59	0·49				
calc.	46·53	2·03	16·74	11·32	0·23	7·73	11·05	3·24	0·52	0·54				0·06
mugearite (MB21.1)→trachyte (MB15.1)														
MB21.1 = 0·39(MB15.1) + 0·12Cpx (En_{33}) + 0·06Ol (Fo_{53}) + 0·38Pl (An_{54}) + 0·04Mt (Usp_{77}) + 0·01Ap														
meas.	50·79	1·78	18·57	9·57	0·18	3·03	8·60	5·39	1·54	0·53				
calc.	50·88	1·61	18·58	9·64	0·23	2·90	8·60	5·24	1·53	0·53				0·08
	Trace element solutions													
	Rb	Sr	Ba	La	Ce	Nd	Sm	Eu	Tb	Yb	Lu	Hf	Ta	Th
MB4.1														
meas.	11	494	199	20·2	44·8	21	5·03	1·81	0·73	1·78	0·26	3·60	1·58	1·7
calc.	12	420	170	25·1	49·8	21	4·61	1·39	0·67	1·53	0·18	3·20	2·07	1·7
D	0·17	0·83	0·16	0·54	0·52	0·62	0·59	0·44	0·59	0·44	0·34	0·44	0·52	0·19
MB21.1														
meas.	31	513	457	43·0	87·5	32	7·46	2·69	1·09	2·96	0·39	6·17	3·64	4·5
calc.	36	512	465	46·3	89·5	37	7·03	3·10	1·02	3·18	0·44	6·93	3·37	4·9
D	0·15	1·88	0·17	0·41	0·38	0·43	0·40	0·86	0·39	0·32	0·27	0·21	0·09	0·14

Bulk distribution coefficients (*D*) for each step of differentiation calculated using published K_D values (Table 5). Cpx, clinopyroxene; Ol, olivine; Pl, plagioclase; Mt, magnetite; Ap, apatite.

a prominent chemical feature of calc-alkaline magmas generated within subduction zones (Thirlwall *et al.*, 1994). Hence, contamination by calc-alkaline compositions may perturb 'normal' OIB-type trace element signatures in alkaline magmas. A potential subduction-related 'contaminant' is the Ford Granodiorite (Weaver *et al.*, 1991, 1992); a biotite-rich, hornblende-bearing granodiorite–monzogranite suite found ~450 km to the west of Mt Sidley in the Ford Ranges. Although Ford Granodiorite is not exposed near Mt Sidley, several granitoid xenoliths collected at Mt Sidley are chemically similar, suggesting that it may occur at depth.

Geochemical variations of the *LT*-trachytes can be explained by assimilation of Ford Granodiorite and fractional crystallization (AFC). Ford Granodiorite $^{87}Sr/^{86}Sr$ and $^{143}Nd/^{144}Nd$ ratios, recalculated to 5 Ma, range from 0·7105 to 0·7361 and 0·51227 to 0·51233, respectively, and are more radiogenic than Mt Sidley volcanic rocks (Table 4) and lower-crustal xenoliths (Wysoczanski, 1993). Mt Sidley samples with elevated $^{87}Sr/^{86}Sr_i$ (Fig. 11a) and low $^{143}Nd/^{144}Nd_i$ (Fig. 11b) lie along AFC trends calculated using a Ford Granodiorite contaminant and model magma compositions derived by 80% fractional crystallization of Sidley basanite and Waesche alkali basalt. Sr, Nd and Nb concentrations predicted by FC curves at 20% magma remaining ($F=0·2$; Fig. 11) are comparable with measured values of phonolitic and trachytic compositions. During Mt Sidley magma genesis, Sr is compatible because of fractionation of plagioclase. D^{Sr} values increase from 1·7 to 4·0 in model differentiation trends (Fig. 11a) marking the onset of alkali feldspar fractionation. Assimilation of granodiorite by highly differentiated magmas at low mass assimilation to mass crystallization rates ($r=0·01$–$0·3$) and moderate to high F values ($\geq 0·3$ on AFC curves) can produce high $^{87}Sr/^{86}Sr_i$–low Sr (<150 p.p.m.) and low $^{143}Nd/^{144}Nd_i$–high Nb (>200 p.p.m.) samples.

Yet this scenario fails to account for the low Nb concentrations (<200 p.p.m.) of the *LT*-trachytes. For instance, in Fig. 11b, an AFC evolutionary path cannot extend below the Nb content of the initial magma, assuming that D^{Nb} is $\ll 1$. Thus, assimilation by differentiated magmas will produce compositions that evolve away from the *LT*-trachyte field. This suggests that low Nb–low $^{143}Nd/^{144}Nd_i$ samples are best explained by AFC involving less fractionated magmas. To illustrate, alkali basalt (sample K19; Table 3) incorporating granodiorite at elevated assimilation rates ($r=0·9$) can account for samples with low $^{143}Nd/^{144}Nd_i$ and Nb concentrations <100 p.p.m. This model closely approximates the composition of DPM in Fig. 11. The apparent discrepancy between this explanation and the previous models requiring contamination of highly evolved magmas to explain low Sr–high $^{87}Sr/^{86}Sr_i$ samples in Fig. 11a can be reconciled by considering trace element and isotopic effects of AFC. Initially, basaltic magmas are buffered against significant changes in Sr isotopic composition because of the high Sr abundance in the initial magmas relative to the assimilant. Because $D^{Sr}>1$, as crystal fractionation proceeds Sr concentrations decrease and the resultant magmas become more sensitive to contamination. This effect is clearly demonstrated by the models presented in Fig. 11a, where high $^{87}Sr/^{86}Sr$ values are limited to low-Sr samples (<150 p.p.m.). In contrast, Nd behaves incompatibly with differentiation and its abundance in basaltic compositions is roughly equivalent to that of the contaminant. Hence in AFC model calculations, contaminated basaltic magmas are displaced towards the Nd isotopic composition of the wallrock much more efficiently than are contaminated, highly evolved magmas. On a graph of $^{143}Nd/^{144}Nd$ versus a highly incompatible element (i.e. Nb and Ta), AFC curves will be steeper for less evolved magmas and flatten out for more evolved compositions. This effect is accentuated with changes in the rate of assimilation to crystal fractionation (r). High r values are suggested for basaltic AFC trends whereas low r paths fit more evolved compositions (inset Fig. 11b). This may be explained by differentiation of basaltic magmas at deep levels in the crust, where high ambient wallrock temperatures and hot basic magmas would facilitate higher rates of assimilation (Davidson & Wilson, 1989; Shaw *et al.*, 1993; Reiners *et al.*, 1995).

To further test and refine the roles of initial magma compositions and granodiorite contaminant in Mt Sidley magma genesis, model differentiation trends are used to predict high LILE/HFSE ratios of *LT*-trachytes. AFC model curves presented in Fig. 12 can adequately explain the shift towards higher K/Ta ratios in *LT*-trachytes and DPM samples. The convolute trends emanating from basalt towards Ford Granodiorite compositions bend at a point (F~0·8–0·7) where the relative enrichment of Ta exceeds that of K (e.g. as F becomes small, ~0·7→0, Ta concentrations are enriched by a factor twice that of K). Several interdependent variables control the relative abundance of an element in a magma experiencing AFC and hence the shape and position of inflection in Fig. 12. Our calculations require high values of r (0·9), low Nb contents in both the assimilant and the initial magma (C_a~Ford Granodiorite and $C°_m$~Waesche alkali basalt, respectively, $C_a/C°_m \sim 1$) and low bulk distribution coefficients ($D^K<1$) to best fit high-K/Ta–low-Nb data. This model offers a hypothetical magma history linking alkali basalt (sample K19) to DPM (as in Fig. 11) and *LT*-trachyte compositions.

Progressive fractionation of *LT*-trachyte magmas may explain high incompatible trace element concentrations in the *HT*-trachyte rocks. Yet, because of the chemical diversity of *LT*-trachytes and the complexity posed by multiple open system processes, models describing the

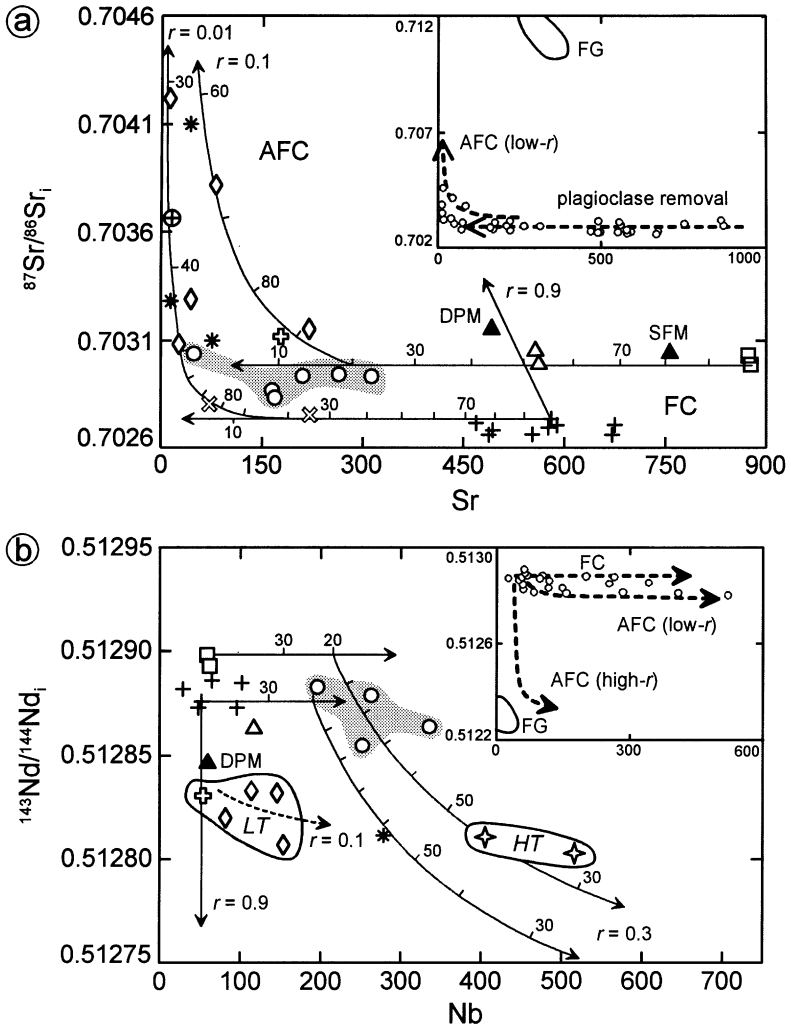

Fig. 11. Graphical presentation of FC and assimilation–fractional crystallization (AFC) models. (a) Plot of initial $^{87}Sr/^{86}Sr$ vs Sr (p.p.m.). Horizontal FC trends from basanite (squares) and alkali basalt (solid crosses) calculated with $D^{Sr}=1{\cdot}7$. Model AFC curves calculated after DePaolo (1981) use Ford Granodiorite (FG) as an assimilant (sample R7460, Weaver *et al.*, 1992; $^{87}Sr/^{86}Sr_{(5)}=0{\cdot}71174$, $^{143}Nd/^{144}Nd_{(5)}=0{\cdot}512279$, Sr = 306, Nd = 33·4 and Nb = 15 p.p.m.) and model magma compositions derived by 80% crystallization of basanite and alkali basalt (samples MB27.5 and K19, respectively; Tables 4 and 5) at low mass assimilation to mass crystallization rates ($r \leq 0{\cdot}1$) and $D^{Sr}=4{\cdot}0$. Assimilation of granodiorite by alkali basalt at $r=0{\cdot}9$ and $D^{Sr}=1{\cdot}7$ approximates DPM. (b) Plot of initial $^{143}Nd/^{144}Nd$ vs Nb (p.p.m.). Generated FC and AFC trends use the same contaminant and modeled compositions as in (a), with $D^{Nd}=0{\cdot}5$ and $D^{Nb}=0{\cdot}2$. The dashed arrow from *LT*-trachyte field represents a generalized AFC trend with $r=0{\cdot}1$. In (a) and (b), numbered tick-marks along FC and AFC curves refer to percent magma remaining. *, Samples from a mixed phonolite–trachyte, black pyroclastic fall deposit. *HT* and *LT* refer to trachyte types presented in Fig. 9. Other symbols are the same as in previous figures.

petrogenesis of *HT*-trachytes cannot be suitably constrained. We propose that further assimilation at low values of *r* (refer to the dashed AFC trend at $r=0{\cdot}1$ in Fig. 11b) could produce the low Nd isotopic ratios and high incompatible trace element contents of *HT*-trachytes.

MAGMA ORIGIN AND PHYSICAL MODELS OF EVOLUTION

The complex geochemical variations of Mt Sidley volcanic rocks are best explained by magmatic differentiation along three major lineages: (1) fractional crystallization of basanite (*ne*>10%) to produce the phonolite series; (2) fractional crystallization of alkali basalt (*ne*<8%) to produce the *N*-trachyte suite; (3) assimilation of crust by alkali basalt and concurrent crystal fractionation evolving *LT*- and *HT*-trachyte compositions. Magma mixing or mingling and the assimilation of wallrock in upper-crustal chambers may account for some enigmatic variations within each series; however, these effects are secondary in terms of controlling the main trends of differentiation. The apparent change in parental magma composition from basanite to alkali basalt reflects a shift towards

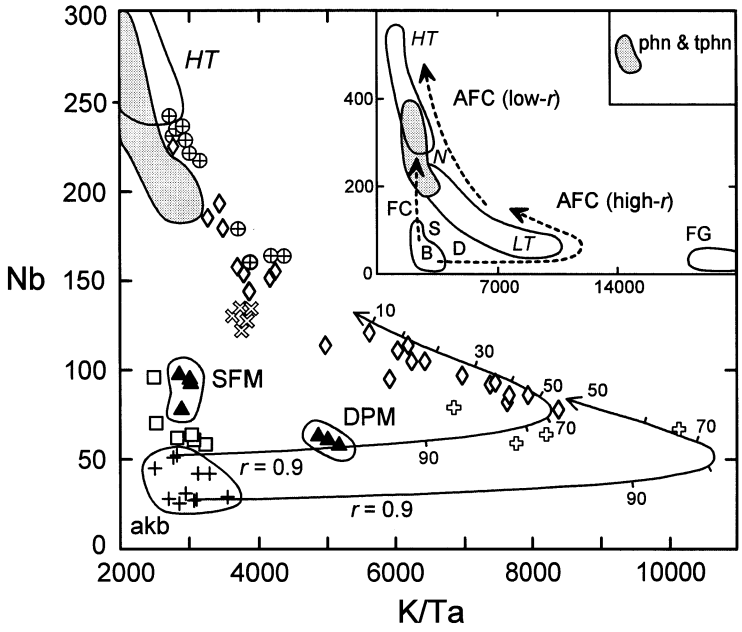

Fig. 12. Plot of Nb (p.p.m.) vs K/Ta showing model AFC curves. The two convolute trends describe the contamination of alkali basalts by Ford granodiorite. Model calculations use alkali basalt MB4.1 (lower curve) and K19 (upper curve), granodiorite as in Fig. 11, $r = 0{\cdot}9$, and $D^{K} = 0{\cdot}5$, $D^{Ta} = 0{\cdot}2$ and $D^{Nb} = 0{\cdot}2$. Inset shows Ford Granodiorite relative to volcanic rocks and general FC and AFC trends. Abbreviations: B, alkali basalt and basanite; D, DPM; S, SFM; phn and tphn, phonolite and tephriphonolite, respectively; *N*, *HT* and *LT*, trachyte types as in Fig. 9.

higher degrees of partial melting of mantle peridotite. Different degrees of partial melting may be the fundamental basis for the divergent petrogeneses of Mt Sidley magmas.

Partial melting and magma ascent

The REE contents of basanitic lavas suggest they can be generated by low degrees of melting (<1%) of a 'depleted' peridotite (Frey & Roden, 1987; Haase & Devey, 1994). In Fig. 13, liquid lines are calculated by non-modal equilibrium batch melting of mantle peridotite. Liquids calculated using a spinel lherzolite from the Executive Committee Range (sample 40E; Wysoczanski, 1993) show that 2% melting with a clinopyroxene/garnet ratio of between 4/1 and 9/1 in the residual will approximate primary basanite compositions (Fig. 13). The production of Mt Waesche alkali basalt involves higher degrees of partial melting (≥ 5) leaving a clinopyroxene/garnet ratio of between 4/1 and 6·5/1.

Small-degree volatile-charged alkaline melts that rise rapidly to the surface will undergo minimal fractionation and interaction with the lithosphere. Mt Sidley basanites, although slightly evolved, are not contaminated by crust; furthermore, the presence of peridotite and pyroxenite xenoliths attests to their rapid ascent. A low-pressure environment for differentiation to phonolite is inferred from normative mineralogy (Panter, 1995). Long-term residence within upper-crustal chambers would probably facilitate magma–wallrock interaction; however, the isotopic and trace element signatures of phonolitic lavas show no contamination by crust (Table 4; Fig. 11). This may reflect the low assimilation potential of magmas surrounded by 'cold' country-rock in shallow reservoirs. In this case, a large magma-wallrock thermal contrast would promote rapid heat loss by conduction and decrease the rate ratio r in AFC models (Reiners *et al.*, 1995). Another explanation could be the lack of a strong compositional dissimilarity between magma and wallrock; a situation that would most probably occur within alkaline rocks of the uppermost Marie Byrd Land crust. Magma storage near the surface may be facilitated by horizons of neutral buoyancy within a volcanic pile. Ryan (1987) suggested that magma stored in equilibrium with ambient density must also be in mechanical equilibrium with its surroundings, thus providing long-term stability to the system. Such a mechanism may explain the ~1 m.y. eruptive history of Mt Sidley phonolites.

Higher degrees of partial melting will produce more silica-saturated volatile-poor basaltic melts (Green, 1971). A more saturated melt may rise more slowly to the surface than a strongly undersaturated melt, providing a greater opportunity for magmas to interact with the lithosphere (see Hoernle & Schmincke, 1993). Mt Waesche alkali basalts, which represent higher degrees of partial melting (up to 10% from a spinel lherzolite,

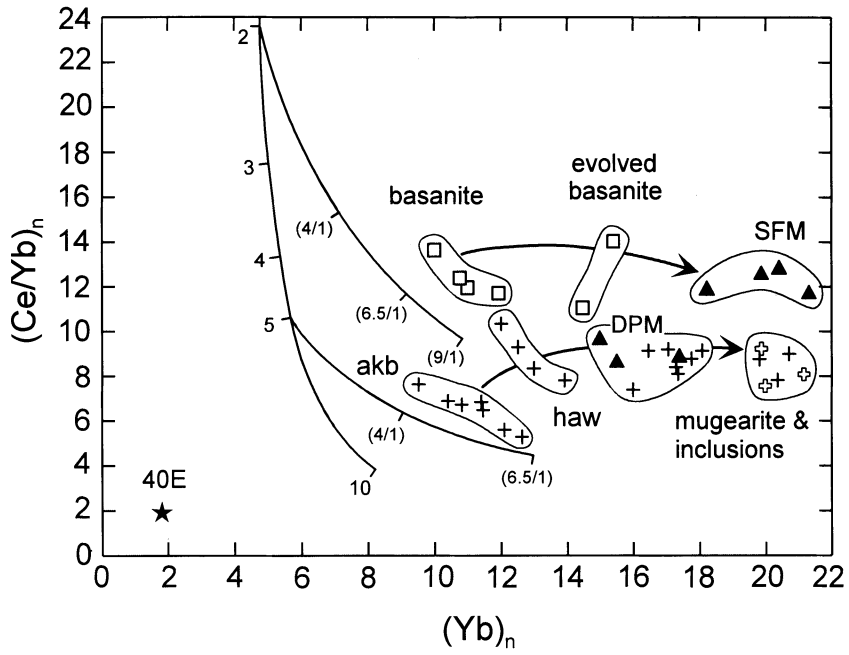

Fig. 13. Plot of chondrite-normalized Yb vs normalized Ce/Yb for Mt Sidley and Mt Waesche basalts and mugearites. Arrows linking compositional fields illustrate two major magmatic lineages; basanite→SFM and alkali basalt→DPM compositions. Continuous lines at left represent non-modal equilibrium batch melting (Shaw, 1970) of a spinel lherzolite (sample 40E; Wysoczanski, 1993). Partial melting lines are calculated using K_D values from Johnson *et al.* (1990), a melting mode of 5% ol, 5% opx, 50% cpx, 40% gt, and a residual mineralogy of 65% ol, 20% opx, 10% cpx, 5% gt. Secondary curves that branch to the right are for higher residual cpx/gt ratios (4/1, 6·5/1, 9/1) calculated at a constant percent of partial melting (denoted by numbered tick marks along the primary curve). Open crosses represent mafic inclusions from commingled lavas.

Fig. 13), contain abundant upper-crustal xenoliths yet inclusions of lowermost crust or mantle are notably absent (Wysoczanski, 1993). This suggests that magmas may have fractionated at mid-crustal levels en route to the surface. Mantle-derived melts that pool at deeper levels in the crust where ambient temperatures are higher will probably experience AFC, suffering significant elemental and isotopic changes only if the assimilant is geochemically distinct from the magma. Such a scenario could explain the origin of the *LT*-trachyte rocks.

Chemical zonation and eruption of trachyte magmas

The ascent of alkali basalts through the lithosphere was arrested at a level where reaction with crust could occur at high assimilation to fractional crystallization rates (r= 0·9). Based on isenthalpic AFC calculations, Reiners *et al.* (1995), determined that high r values (≥ 1) can result during early stages of basalt contamination when initial country rock temperatures are between 400 and 800°C. A high geothermal gradient within the Marie Byrd Land crust may be inferred by the presence of young volcanic centers (LeMasurier & Thomson, 1990), active volcanism (Blankenship *et al.*, 1993) and by analogy with the western Ross Sea (Berg *et al.*, 1989; Della Vedova *et al.*, 1992).

The emplacement of AFC-derived trachytic compositions within an upper-crustal reservoir allowed for the chemical stratification of the magma. In Fig. 14, we illustrate *LT*-trachyte magma passing upward into *HT*-trachyte magma, implying strong roofward enrichment in Rb, Th, Nb, Ta, Hf, Y, Zr and REE (and volatiles?) and depletion in Al, Ba and Sr. We speculate that differentiation at this stage was dominated by fractionation of alkali feldspar, probably, in concert with very low rates of assimilation.

The eruption of the compositionally zoned system was initiated by explosive interaction between cupola liquids (*HT*-trachyte) and a separate body of phonolitic magma (Fig. 14b). The intrusion of slightly less dense trachytic magma [~2·40 g/cm^3; calculated at 900°C using the method of Bottinga *et al.* (1982)] into phonolite (>2·47 g/cm^3) caused vigorous convection and magma mixing. The geochemical heterogeneity of a black pyroclastic fall deposit (Table 4; Fig. 11) suggests that the interaction between the two magmas occurred shortly before eruption. Injection of trachyte magma into the overlying chamber and the subsequent heating and vesiculation of the resident magma increased fluid pressure sufficiently

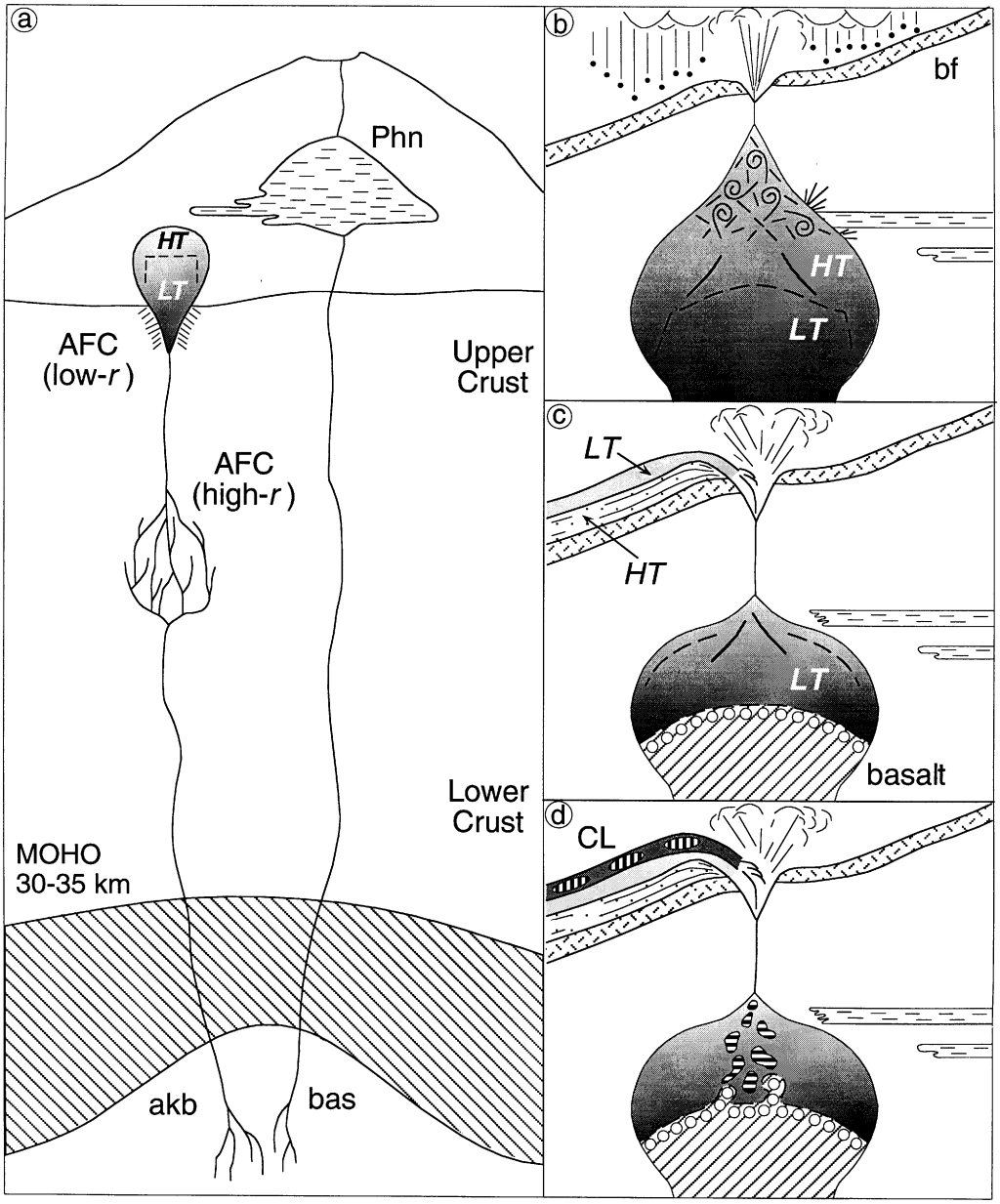

Fig. 14. Model for the chemical zonation and eruption of trachyte magmas. (a) Phonolitic magma-reservoir (Phn) situated within the volcanic edifice at the end of stage I activity (4·8 Ma). Basanitic melts (bas), parental to stage I phonolites, are superseded by alkali basalt (akb) because of an increase in the degree of mantle partial melting. Alkali basalt reacted with granodiorite at high assimilation–fractional crystallization rates (high *r*) to form *LT*-trachytes. Emplacement of *LT*-trachyte magmas into an upper-crustal chamber allowed further differentiation by low-*r* AFC producing *HT*-trachyte magmas. (b) Upper portion of zoned trachytic chamber intrudes a separate body of phonolite causing chamber overpressure and explosive eruption of mixed magmas (phonolite + trachyte) to produce a compositionally heterogeneous black pyroclastic fall deposit (bf). (c) As the pressure in the system decreased, lower discharge rates erupted lavas of *HT*- followed by *LT*-trachyte compositions (4·6 Ma). At some stage, basalt was injected into the chamber and cooled against the overlying magmas. (d) Plumes of vesiculated basalt rose from a layer of gravitational instability and mingled with the overlying *LT*-trachyte magmas and were erupted as commingled lavas (CL).

to fracture the confining chamber walls and drive magmas explosively to the surface. The appearance of a strongly welded black pyroclastic fall deposit may reflect higher accumulation rates near the vent; a consequence of lower eruption column height as the gas content in the magma and its rate of discharge decreased. Such a scenario can explain the passage of the black pyroclastic fall unit up into basal lavas of the *HT*-trachyte suite. As the pressure in

the system decreased and mixing abated, lower discharge rates were driven by volatile exsolution in reservoir magmas, erupting the upper portion of the chamber as lavas (Fig. 14c).

Later the chamber was replenished by basaltic magma which pooled beneath the trachyte magma at the base of the system (Fig. 14c). Initially, mixing of the two magmas was inhibited because of their strong density contrast (see Koyaguchi & Blake, 1991). On the basis of field observations and fluid dynamical concepts, magma mixing in a stratified system may occur if the lower mafic layer becomes vesiculated, which effectively decreases its density until it is equal to that of the overlying magma (Eichelberger, 1980; Huppert *et al.*, 1982, 1984; Thomas *et al.*, 1993). This may occur when hot volatile-rich mafic magma is cooled rapidly against lower-temperature reservoir magma, crystallizing and becoming saturated with respect to volatile components. In laboratory experiments, Thomas *et al.* (1993) demonstrated that gas bubbles moving through a high-viscosity liquid will accumulate below a lower-viscosity less dense liquid and form a layer of gravitational instability, giving rise to bubble plumes which buoyantly ascend and mix with overlying fluids. In Fig. 14d, we adopt the plume theory of mixing for mafic inclusion-bearing lavas of the *LT*-trachyte suite to best explain: (1) the coarse mixture of small (typically $\leq$10 cm) vesiculated inclusions; (2) the lack of hybrid lithologies (homogeneous mixtures); (3) the occurrence of individual small volume inclusion-bearing units. The third observation argues against deposition during a single large eruption triggered by convective overturn (e.g. Sparks *et al.*, 1977; Wolff, 1985; Araña *et al.*, 1994).

CONCLUSIONS

Studies of Mt Sidley permit the dynamic reconstruction of its volcanic history and petrogenesis, and offer an insight into the genetic relations of phonolitic and trachytic magma series within an intraplate continental setting. At Mt Sidley, the spatial and temporal distinction between phonolites and trachytes and their strongly divergent geochemistry have been explained by evolution along separate magma trends. Furthermore, each series appears to have originated from a distinct basaltic parent (i.e. basanite→phonolite, alkali basalt→trachyte).

Major changes in the composition of erupted magmas at each stage of activity can be related to variations in the degree of partial melting in the upper mantle. Our model suggests that basanitic magmas were derived by low ($\leq$2%) degrees of partial melting of a mantle peridotite, whereas alkali basalts required higher (5-10%) degrees of melting of the same source. Hence, the transition from phonolite series compositions of stage I to the trachytes of stage II (*HT*- and *LT*-trachyte suites) must ultimately reflect an increase in the degree of partial melting of the source. The *N*-trachytes, which were erupted at the beginning of stage III, are overlain by DPM tephras (derivatives of alkali basalt) and then by SFM and other intermediate compositions (derivatives of basanite) at the southern end of Mt Sidley. The stage III succession is interpreted as being transitional between higher and lower degrees of partial melting that culminated with the eruption of xenolith-bearing basanite during stage IV.

The variation in the degree of partial melting (low→high→low) during the 1·5 Ma life-span of Mt Sidley is coincident with a southward migration of its activity. The rate and style of migration is emulated on a larger scale by the Executive Committee Range, where the southward displacement of activity corresponds to major changes in the composition of erupted magmas between centers (Panter *et al.*, 1994). Volcanic migration in Marie Byrd Land cannot be explained as traces of individual mantle hot spots, as the Antarctic Plate is stationary (Lawver *et al.*, 1991) and the trends of other linear volcanic chains, which also show progressive younging towards the outer edge of the province (LeMasurier & Rex, 1989), are at 90° to each other. Therefore, the gross surficial expression of volcanism must reflect a horizontal relocation of sub-lithospheric zones of decompressive melting towards the outer edge of the province. The partial melting cycle at Mt Sidley is thus interpreted to reflect the passing influence of a mantle upwelling beneath that portion of the lithosphere. Taking into account the HIMU OIB-like geochemical signature of basaltic samples, volcanism must have tapped a source largely affected by mantle plume activity.

The whole-rock and mineral compositions of Mt Sidley rocks suggest a complex differentiation history within the continental crust. Theoretical modeling of geochemical variations reveals that, whereas crystal–liquid fractionation processes within shallow reservoirs were dominant during phonolite production, AFC played an important role in trachyte genesis and led to the production of silica-oversaturated compositions. We consider this to be a partial function of the rate of ascent through the crust, implying that alkali basaltic melts (parental to trachyte) rose more slowly than basanitic melts (parental to phonolite).

ACKNOWLEDGEMENTS

This study was funded by National Science Foundation Grants DPP-8816342 and OPP-9118806 to P. Kyle and W. McIntosh. Fieldwork on Mt Sidley was completed with the help of W. McIntosh and J. Gamble. Logistical support in Antarctica was provided by USAP and NZAP

personnel and the Navy VXE-6 squadron. We thank R. Pankhurst, A. Campbell and J. Gamble for access to analytical facilities and guidance in producing many of the data shown here. Pb isotope data were generously provided by S. Mukasa. R. Wysoczanski is thanked for providing unpublished xenolith analyses. Constructive comments by J. Marsh, A. Ewart and an anonymous reviewer improved the manuscript.

REFERENCES

Allègre, C. J., Treuil, M., Minster, J. F., Minster, B. & Albarède, F., 1977. Systematic use of trace elements in igneous process, Part I: fractional crystallization processes in volcanic suites. *Contributions to Mineralogy and Petrology* **60,** 57–75.

Araña, V., Martí, J., Aparicio, A., García-Cacho, L. & García-García, R., 1994. Magma mixing in alkaline magmas: an example from Tenerife, Canary Islands. *Lithos* **32,** 1–19.

Arth, J. G., 1976. Behavior of trace elements during magmatic processes—summary of theoretical models and their applications. *Journal of Research of the US Geological Survey* **4,** 41–47.

Berg, J. H., Moscati, R. J. & Herz, D. L., 1989. A petrologic geotherm from a continental rift in Antarctica. *Earth and Planetary Science Letters* **93,** 98–108.

Blankenship, D. D., Bell, R. E., Hodge, S. M., Brozena, J. M., Behrendt, J. C. & Finn, C. A., 1993. Active volcanism beneath the west Antarctic ice sheet and implications for ice-sheet stability. *Nature* **361,** 526–529.

Bottinga, Y., Weill, D. & Richet, P., 1982. Density calculations for silicate liquids I: revised method for aluminosilicate compositions. *Geochimica et Cosmochimica Acta* **46,** 909–919.

Brown, W. L., 1993. Fractional crystallization and zoning in igneous feldspars: ideal water-buffered liquid fractionation lines and feldspar zoning paths. *Contributions to Mineralogy and Petrology* **113,** 115–125.

Caroff, M., Maury, R. C., Leterrier, J., Joron, J. L., Cotten, J. & Guille, G., 1993. Trace element behavior in the alkali basalt–comenditic trachyte series from Mururoa Atoll, French Polynesia. *Lithos* **30,** 1–22.

Coplen, 1994. Reporting of stable hydrogen, carbon, and oxygen isotopic abundances. *Pure and Applied Chemistry* **66,** 273–276.

Cox, K. G., Bell, J. D. & Pankhurst, R. J., 1979. *The Interpretation of Igneous Rocks*. London: Allen & Unwin, 450 pp.

Cox, K. G., Charnley, N., Gill, R. C. O. & Parish, K. A., 1993. Alkali basalts from Shuqra, Yemen: magmas generated in the crust–mantle transition zone? In: Prishard, H. M., Alabaster, T., Harris, N. B. & Neary, C. R. (eds) *Magmatic Processes and Plate Tectonics. Geological Society of London, Special Publication* **76,** 443–453.

Davidson, J. P. & Wilson, I. R., 1989. Evolution of an alkali basalt–trachyte suite from Jebel Marra volcano, Sudan, through assimilation and fractional crystallization. *Earth and Planetary Science Letters* **95,** 141–160.

Deer, W. A., Howie, R. A. & Zussman, J., 1966. *An Introduction to the Rock-Forming Minerals*. London: Longman, 528 pp.

Della Vedova, B., Pellis, G., Lawver, L. A. & Brancolini, G., 1992. Heat flow and tectonics of the western Ross Sea. In: Yoshida, Y., Kaminuma, K. & Shiraishi, K. (eds) *Recent Progress in Antarctic Earth Science*. Tokyo: Terra Scientific, pp. 627–637.

DePaolo, D. J., 1981. Trace element and isotopic effects of combined wallrock assimilation and fractional crystallization. *Earth and Planetary Science Letters* **53,** 189–202.

Eichelberger, J. C., 1980. Vesiculation of mafic magma during replenishment of silicic magma reservoirs. *Nature* **288,** 446–450.

Ernst, W. G., 1962. Synthesis, stability relations, and occurrence of riebeckite and riebeckite–arfvedsonite solid solutions. *Journal of Geology* **70,** 689–736.

Fitton, J. G., 1987. The Cameroon line, west Africa: a comparison between oceanic and continental alkaline volcanism. In: Fitton, J. G. & Upton, B. G. L. (eds) *Alkaline Igneous Rocks. Geological Society of London, Special Publication* **30,** 273–291.

Foland, K. A., Landoll, J. D., Henderson, C. M. B. & Jiangfeng, C., 1993. Formation of cogenetic quartz and nepheline syenites. *Geochimica et Cosmochimica Acta* **57,** 697–704.

Freundt, A. & Schmincke, H.-U., 1995. Petrogenesis of rhyolite–trachyte–basalt composite ignimbrite P1, Gran Canaria, Canary Islands. *Journal of Geophysical Research* **100,** 455–474.

Frey, F. A. & Roden, M. F., 1987. The mantle source for the Hawaiian Islands: constraints from the lavas and ultramafic inclusions. In: Menzies, M. A. & Hawkesworth, C. J. (eds) *Mantle Metasomatism*. London: Academic Press, pp. 423–463.

Frey, F. A., Green, D. H. & Roy, S. D., 1978. Integrated models of basalt petrogenesis: a study of quartz tholeiites to olivine melilites from south eastern Australia utilizing geochemical and experimental petrological data. *Journal of Petrology* **19,** 463–513.

Gourgaud, A., 1991. Comagmatic enclaves in lavas from the Mont-Dore composite volcano, Massif Central, France. In: Didier, J. & Barbarin, B. (eds) *Enclaves and Granite Petrology, Developments in Petrology 13*. Amsterdam: Elsevier, pp. 221–233.

Green, D. H., 1971. Composition of basaltic magmas as indicators of conditions of origin: application to oceanic volcanism. *Philosophical Transactions of the Royal Society of London, Series A* **268,** 707–725.

Haase, K. M. & Devey, C. W., 1994. The petrology and geochemistry of Vesteris Seamount, Greenland Basin—an intraplate alkaline volcano of non-plume origin. *Journal of Petrology* **35,** 295–328.

Hart, S. R. & Kyle, P. R., 1994. The geochemistry of McMurdo Group volcanic rocks. *Antarctic Journal of the United States* **18,** 14–16.

Hart, S. R., Blusztajn, J. S. & Kyle, P. R., 1994. The geochemistry of McMurdo Group volcanic rocks, Antarctica. ICOG8, Berkeley, CA. *US Geological Survey Circular* **1107,** 130.

Hoernle, K. & Schmincke, H.-U., 1993. The role of partial melting in the 15-Ma geochemical evolution of Gran Canaria: a blob model for the Canary hotspot. *Journal of Petrology* **34,** 599–626.

Hole, M. J. & LeMasurier, W. E., 1994. Tectonic controls on the geochemical composition of Cenozoic mafic alkaline volcanic rocks from West Antarctica. *Contributions to Mineralogy and Petrology* **117,** 187–202.

Huppert, H. E., Sparks, R. S. J. & Turner, J. S., 1982. Effects of volatiles on mixing in calc-alkaline magma systems. *Nature* **297,** 554–557.

Huppert, H. E., Sparks, R. S. J. & Turner, J. S., 1984. Some effects of viscosity on the dynamics of replenished magma chamber. *Journal of Geophysical Research* **89,** 6857–6877.

James, D. E., 1981. The combined use of oxygen and radiogenic isotopes as indications of crustal contamination. *Annual Review of Earth and Planetary Science* **9,** 311–344.

Johnson, K. T. M., Dick, H. J. B. & Shimizu, N., 1990. Melting in the oceanic upper mantle: an ion microprobe study of diopsides in abyssal peridotites. *Journal of Geophysical Research* **95,** 2661–2678.

Koyaguchi, T. & Blake, S., 1991. Origin of mafic enclaves: constraints on the magma mixing model from fluid dynamic experiments. In: Didier, J. & Barbarin, B. (eds) *Enclaves and Granite Petrology, Developments in Petrology 13*. Amsterdam: Elsevier, pp. 415–429.

Kyle, P. R., 1981. Mineralogy and geochemistry of a basanite to phonolite sequence at Hut Point Peninsula, Antarctica, based on

core from Dry Valley Drilling Project drillholes 1, 2, and 3. *Journal of Petrology* **22,** 451–500.

Kyle, P. R., 1986. Mineral chemistry of Late Cenozoic McMurdo Volcanic Group rocks from The Pleiades, northern Victoria Land. In: Stump, E. (ed.) *Geological Investigations in Northern Victoria Land, Antarctic Research Series, Vol. 46*. Washington, DC: American Geophysical Union, pp. 305–337.

Kyle, P. R., Moore, J. A. & Thirlwall, M. F., 1992. Petrologic evolution of anorthoclase phonolite lavas at Mount Erebus, Ross Island, Antarctica. *Journal of Petrology* **33,** 849–875.

Kyle, P. R., Pankhurst, R., Mukasa, S., Panter, K., Smellie, J. & McIntosh, W., 1994. Sr, Nd and Pb isotopic variations in the Marie Byrd Plume, West Antarctica. ICOG8, Berkeley, CA. *US Geological Survey Circular* **1107,** 184.

Langmuir, C. H., Vocke, R. D., Hanson, G. N. & Hart, S. R., 1978. A general mixing equation with applications to Icelandic basalts. *Earth and Planetary Science Letters* **37,** 380–392.

Larsen, L. M., 1976. Clinopyroxene and coexisting mafic minerals from the alkaline Ilímaussaq intrusion, south Greenland. *Journal of Petrology* **17,** 258–290.

Larsen, L. M., 1979. Distribution of REE and other trace elements between phenocrysts and peralkaline undersaturated magmas, exemplified by rocks from the Gardar igneous province, south Greenland. *Lithos* **12,** 303–315.

Lawver, L. A., Royer, J. Y., Sandwell, D. T. & Scotese, C. R., 1991. Evolution of the Antarctic continental margin. In: Thompson, M. R. A., Crame, J. A. & Thomson, J. W. (eds) *Geological Evolution of Antarctica*. Cambridge: Cambridge University Press, pp. 533–539.

Le Bas, M. J., Maitre, R. W., Streckeisen, A. & Zanettin, B., 1986. A chemical classification of volcanic rocks based on the total alkali–silica diagram. *Journal of Petrology* **27,** 745–750.

LeMasurier, W. E. & Rex, D. C., 1989. Evolution of linear volcanic ranges in Marie Byrd Land, west Antarctica. *Journal of Geophysical Research* **94,** 7223–7236.

LeMasurier, W. E. & Thomson, J. W., 1990. *Volcanoes of the Antarctic Plate and Southern Oceans. Antarctic Research Series 48*. Washington, DC: American Geophysical Union, 487 pp.

Macdonald, R., Davies, G. R., Upton, B. G. J., Dunkley, P. N., Smith, M. & Leat, P. T., 1995. Petrogenesis of Silali volcano, Gregory Rift, Kenya. *Journal of the Geological Society of London* **152,** 703–720.

Mogessie, A., Tessadri, R. & Veltman, C. B., 1990. EMP-AMPH—a hypercard program to determine the name of an amphibole from electron microprobe analysis according to the International Mineralogical Association scheme. *Computers and Geosciences* **16,** 309–330.

Morimoto, N., Fabries, J., Ferguson, A. K., Ginzburg, I. V., Ross, M., Seifert, F. A., Zussman, J., Aoki, K. & Gottardi, G., 1988. Nomenclature of pyroxenes. *Mineralogy and Petrology* **39,** 55–76.

Mukasa, S. B., Shervais, J. W., Wilshire, H. G. & Nielson, J., 1991. Intrinsic isotopic heterogeneities exhibited by the Lherz alpine peridotite massif, French Pyrenees. *Journal of Petrology* (Special Lherzolites Issue), 117–134.

Panter, K. S., 1995. Geology, geochemistry and petrogenesis of the Mount Sidley volcano, Marie Byrd Land, Antarctica. Ph.D. Thesis, New Mexico Institute of Mining and Technology, Socorro, 210 pp.

Panter, K. S., McIntosh, W. C. & Smellie, J. L., 1994. Volcanic history of Mount Sidley, a major alkaline volcano in Marie Byrd Land, Antarctica. *Bulletin of Volcanology* **56,** 361–376.

Reiners, P. W., Nelson, B. K. & Ghiorso, M. S., 1995. Assimilation of felsic crust by basaltic magma: thermal limits and extents of crustal contamination of mantle-derived magmas. *Geology* **23,** 563–566.

Roeder, P. L. & Emslie, R. F., 1970. Olivine–liquid equilibrium. *Contributions to Mineralogy and Petrology* **29,** 275–289.

Ryan, M. P., 1987. Neutral buoyancy and the mechanical evolution of magmatic systems. In: Mysen, B. O. (ed.) *Magmatic Processes: Physicochemical Principles. Geochemical Society, Special Publication* **1,** 259–287.

Shaw, A., Downes, H. & Thirlwall, M. F., 1993. The quartz-diorites of Limousin: elemental and isotopic evidence for Devono-Carboniferous subduction in the Hercynian belt of the French Massif Central. *Chemical Geology* **107,** 1–18.

Shaw, D. M., 1970. Trace element fractionation during anatexis. *Geochimica et Cosmochimica Acta* **50,** 711–724.

Smellie, J. L., McIntosh, W. C., Gamble, J. A. & Panter, K. S., 1990. Preliminary stratigraphy of volcanoes in the Executive Committee Range, central Marie Byrd Land. *Antarctic Science* **2,** 353–354.

Sparks, R. S. J., Sigurdsson, H. & Wilson, L., 1977. Magma mixing: a mechanism for triggering acid explosive eruptions. *Nature* **267,** 315–318.

Stephenson, D. & Upton, B. G. J., 1982. Ferromagnesian silicates in a differentiating alkaline complex: Kûngnât Fjeld, south Greenland. *Mineralogical Magazine* **46,** 283–300.

Stimac, J. A. & Pearce, T. H., 1992. Textural evidence of mafic–felsic magma interaction in dacite lavas, Clear Lake, California. *American Mineralogist* **77,** 795–809.

Sun, S. & McDonough, W. F., 1989. Chemical and isotopic systematics of oceanic basalts: implications for mantle composition and processes. In: Saunders, A. D. & Norry, M. J. (eds) *Magmatism in the Ocean Basins. Geological Society of London, Special Publication* **42,** 313–345.

Thirlwall, M. F., Smith, T. E., Graham, A. M., Theodorou, N., Hollings, P., Davidson, J. P. & Arculus, R. J., 1994. High field strength element anomalies in arc lavas: source or process? *Journal of Petrology* **35,** 819–838.

Thomas, N., Tait, S. & Koyaguchi, T., 1993. Mixing of stratified liquids by the motion of gas bubbles: application to magma mixing. *Earth and Planetary Science Letters* **115,** 161–175.

Thompson, R. N., Morrison, M. A., Hendry, G. L. & Parks, S. J., 1984. An assessment of the relative roles of crust and mantle in magma genesis: an elemental approach. *Philosophical Transactions of the Royal Society of London, Series A* **310,** 549–590.

Treuil, M. & Joron, J. M., 1975. Utilisation des éléments hygromagmatophiles pour la simplification de la modèlisation quantitative des processus magmatiques, exemples de l'Afar et de la dorsade médioatlantique. *Rendiconti della Societá Italiana di Mineralogia e Petrologia* **31,** 125–174.

Turbeville, B. N., 1993. Petrology and petrogenesis of the Latera Caldera, central Italy. *Journal of Petrology* **34,** 77–123.

Tuttle, O. F. & Bowen, N. L., 1958. Origin of granite in the light of experimental studies in the system $NaAlSi_3O_8$–$KAlSi_3O_8$–SiO_2–H_2O. *Geological Society of America, Memoir* **74,** 153 pp.

Ulmer, P., 1989. The dependence of the Fe^{2+}–Mg cation-partitioning between olivine and basaltic liquid on pressure, temperature and composition. An experimental study to 30 kbars. *Contributions to Mineralogy and Petrology* **101,** 261–273.

Weaver, B. L., 1991. Trace element evidence for the origin of ocean-island basalts. *Geology* **19,** 23–26.

Weaver, S. D., Bradshaw, J. D. & Adams, C. J., 1991. Granitoids of the Ford Ranges, Marie Byrd Land, Antarctica. In: Thompson, M. R. A., Crame, J. A. & Thomson, J. W. (eds) *Geological Evolution of Antarctica*. Cambridge: Cambridge University Press, pp. 345–351.

Weaver, S. D., Adams, C. J., Pankhurst, R. J. & Gibson, I. L., 1992. Granites of Edward VII Peninsula, Marie Byrd Land: anorogenic magmatism related to Antarctic–New Zealand rifting. *Transactions of the Royal Society of Edinburgh* **83,** 281–290.

Weaver, S. D., Storey, B. C., Pankhurst, R. J., Mukasa, S. B., DiVenere, V. J. & Bradshaw, J. D., 1994. Antarctica–New Zealand rifting and Marie Byrd Land lithospheric magmatism linked to ridge subduction and mantle plume activity. *Geology* **22,** 811–814.

Wilson, M., Downes, H. & Cebriá J., 1995. Contrasting fractionation trends in coexisting continental alkaline magma series; Cantal, Massif Central, France. *Journal of Petrology* **36,** 1729–1753.

Wolff, J. A., 1985. Zonation, mixing and eruption of silica-undersaturated alkaline magma: a case study from Tenerife, Canary Islands. *Geological Magazine* **122,** 641–647.

Wolff, J. A. & Toney, J. B., 1993. Trapped liquid from a nepheline syenite: a re-evaluation of Na-, Zr-, F-rich interstitial glass in a xenolith from Tenerife, Canary Islands. *Lithos* **29,** 285–293.

Wood, D. A., Tarney, J. & Weaver, B. L., 1981. Trace element variations in Atlantic Ocean basalts and Proterozoic dykes from northwest Scotland: their bearing upon the nature and geochemical evolution of the upper mantle. *Tectonophysics* **75,** 91–112.

Woodhead, J. D., 1996. Extreme HIMU in an oceanic setting: the geochemistry of Mangaia Island (Polynesia), and temporal evolution of the Cook–Austral hostspot. *Journal of Volcanology and Geothermal Research* **72,** 1–19.

Wysoczanski, R. J., 1993. Lithospheric xenoliths from the Marie Byrd Land volcanic province, west Antarctica. Ph.D. Thesis, Victoria University of Wellington, New Zealand, 475 pp.

Zindler, A. & Hart, S., 1986. Chemical geodynamics. *Annual Review of Earth and Planetary Science* **14,** 493–571.